Summer 2020

Control of Voltage-Source Converters Considering Virtual Inertia Dynamics

Tri Nguyen

CONTROL OF VOLTAGE-SOURCE CONVERTERS CONSIDERING

VIRTUAL INERTIA DYNAMICS

by

TRI NGUYEN

(Under the Direction of Masoud Davari)

ABSTRACT

Controlling power-electronic converters in power systems has significantly gained more attention due to the rapid penetration of alternative energy sources. This growth in the depth of penetration also poses a threat to the frequency stability of modern power systems. Photovoltaic and wind power systems utilizing power-electronic converters without physical rotating masses, unlike traditional power generations, provide low inertia, resulting in frequency instability. Different research has developed the control aspects of power-electronic converters, offering many control strategies for different operation modes and enhancing the inertia of converter-based systems. The precise control algorithm that can improve the inertial response of converter-based systems in the power grid is called virtual inertia. This thesis employs a control methodology that mimics synchronous generators characteristics based on the swing equation of rotor dynamics to create virtual inertia. The models are also built under different cases, including grid-connected and islanded situations, using the swing equation with inner current and voltage outer loops. Analysis of the simulation results in MATLAB/Simulink demonstrates that active and reactive power are independently controlled under the grid-imposed mode, voltage and frequency are controlled under the islanded mode, and frequency stability of the system is enhanced by the virtual inertia em-

ulation using the swing equation. On this basis, it is recommended that the swing equation-based approach is incorporated with the current and voltage control loops to achieve better protection under over-current conditions. Further works are required to discover other factors that can improve the effectiveness of the models.

INDEX WORDS: Virtual inertia, Swing equation, Current-Controlled, Voltage controller, Grid-Connected, Islanded.

CONTROL OF VOLTAGE-SOURCE CONVERTERS CONSIDERING VIRTUAL INERTIA DYNAMICS

by

TRI NGUYEN

B.Sc., Da Nang University of Technology, Vietnam, 2018

A Thesis Submitted to the Graduate Faculty of Georgia Southern University in Partial Fulfillment of the Requirements for the Degree

MASTER OF SCIENCE

CONTROL OF VOLTAGE-SOURCE CONVERTERS CONSIDERING VIRTUAL INERTIA DYNAMICS

by

TRI NGUYEN

Major Professor:	Masoud Davari
Committee:	Rocio Alba-Flores
	Weinan Gao
	Seungmo Kim

Electronic Version Approved:
July 2020

DEDICATION

This thesis is dedicated to my family.

ACKNOWLEDGMENTS

I want to express my heartiest gratitude to my advisor, Dr. Masoud Davari, who has always been supportive through my research. I appreciate all his contributions to time, efforts, ideas, and financial support during my program. It has been an honor to be the first master student who graduates under his supervision. Also, I thank the committee members for reviewing my thesis and providing me with constructive, insightful feedback. Last but not least, I would also like to acknowledge the financial support of the U.S. National Science Foundation (NSF) through Grants #1902787 provided by the Core Program of Energy, Power, Control, and Networks (EPCN) in the Division of Electrical, Communications and Cyber Systems (ECCS).

TABLE OF CONTENTS

LIST OF TABLES

LIST OF FIGURES

LIST OF SYMBOLS

Symbol	Description	Symbol	Description
$< ., . >$	Inner product of two vectors in $\mathbb{R}^3$	$\widetilde{(.)}$	Vector comprising three 120^0 out of phase components
$\widehat{a}$	Amplitude of vector $\overrightarrow{a}$	$\pounds()$	Laplace transform operator
θ	Phase angle	ρ	Angular position
ω	Angular velocity	ω_g	Angular velocity of the grid
$\Delta\omega$	Difference of nominal and grid angular velocity	D	Damping factor
J	Moment of inertia	P	Active power
P_m	Mechanical power	P_e	Electrical power
Q	Reactive power	R	Connection Resistance
L	Filter inductance	C_f	Filter capacitance
T_e	Electromagnetic torque	T_m	Mechanical torque
I_d	d-axis component of current	I_q	q-axis component of current
V_d	d-axis component of voltage	I_q	q-axis component of voltage
v_c	Carrier voltage	v_m	Modulation voltage
D_p	Frequency drooping coefficient	D_q	Voltage droop coefficient
k_P	Proportional gain	k_I	Integral gain
S	Apparent power	$M_f i_f$	Field excitation

CHAPTER 1

INTRODUCTION

The utilization of alternative energy sources has been promoted in the modern power system to solve the energy crisis and global warming [1, 2]. The current power grid is connected to not only traditional power plants, including thermal and hydropower plants, but also numerous solar panels and wind turbine generators. As specified by the International Energy Agency (IEA), global renewable power generation capacity is estimated to rise by 50% of 1,200 GW between 2019 and 2024, which is corresponding to the entire installed capacity of the United States currently [3]. Solar photovoltaic (PV) was still leading the installed renewable power capacity statistics with 100 GW added, accounting for 55% of new renewable capacity, followed by wind power (28%) in 2018. In total, alternative energy constitutes over 33% of the world's installed power generating capacity in 2018 [4]. Due to the substantial increasing demand in PV and wind power with DC loads, the power system is gravitated towards an inverter-dominated network and further an AC/DC hybrid grid with large DC-energy pools [5]. Despite fast response time, the inverters as static converters lack the mechanical spinning component, thus do not possess the same moment of inertia as synchronous generators to reinforce the grid dynamics.

Consequently, the large-scale penetration of renewable energy sources lowers the total inertia of the network and threatens the power system's stability. Various potential solutions have been proposed, such as running multiple synchronous generators at partial load conditions or using grid-scale energy storage devices. Despite being useful in inertia sustainability or fast response to frequency events, there are still many disadvantages like higher operating costs, low round-trip efficiency, limited life-cycle, safety, and noises [6, 7]. The idea of implementing virtual inertia for an inverter-based system has been pointed towards by many researchers as a solution for the power system stability to cope with the increasing penetration of alternative power generation using inverters [8, 9].

1.1 Motivation

In a power grid, according to physics, frequency is an indicator of the match between load consumption and power generation. Any alteration in the active power generation or the power consumption results in power imbalance and deviation in the frequency. Conventionally, synchronous generators in traditional power plants play a crucial role in sustaining dynamic frequency stability as they behave like energy storage. Kinetic energy is absorbed or released by the rotating masses of the synchronous generators during the time of frequency deviation. Such a property of rotating masses to resist the sudden deviation in frequency is named as the moment of inertia. The higher the total inertia of the network is, the slower the dynamics of frequency change is, which effectively avoids unpredictable load-shedding, cascading failures, or large-scale blackouts [10]. However, there is no mechanical spinning component in static inverters. Hence, these grid-connected inverters do not contribute inertia to the electrical grid, leading to inadequate inertial response of the power system [11]. The primary governor might not adapt quickly enough to the frequency fluctuations. This issue can be detected and measured by frequency tripping protective relay if the deviation is $\pm 0.5\%$, falling in between 59.7Hz and 60.3Hz for a 60Hz grid. The tripping of the circuit breaker, disconnecting the generators from the network, results in system instability. Consequently, this restricts the maximum amount of grid-connected non-synchronous systems.

A multiple time-frame frequency response in a power system has been simulated to show a clearer sight of how frequency recovery is, in the presence of virtual inertia and vice versa, illustrated in Figure 1.1 [12]. As can be seen, the first 10 seconds after the frequency event determine how well the system inertia can slow down the dynamics of frequency change and reduce the frequency deviations. It shows that the reduction in frequency nadir (minimum frequency point) can be compensated by additional virtual inertia, and the rate of change of frequency (ROCOF) has improved significantly. The primary control of the

governor is only taken into action within 10-30s after the inertial response time. This process is not instantaneous enough to arrest the system frequency. Thus, the virtual inertia concept has been researched and developed.

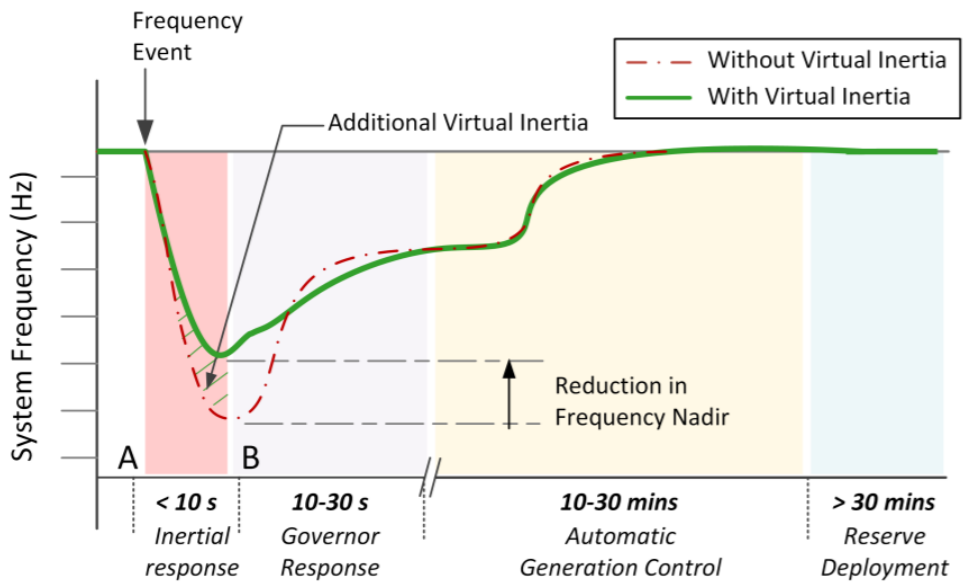

Figure 1.1: Multiple Time-Frame Frequency Response Following a Frequency Event

Numerous control algorithms for implementing virtual inertia into the inverter-based system are presented in the literature review in the next chapter. Most of the latest approaches with various topologies are discussed to summarize and classify in the concept of virtual synchronous machine (VSM) according to their functional characteristics and controller designs.

1.2 Contribution

This thesis's main contribution is a control strategy that implements the virtual inertia for the voltage-source converters under grid-connected and islanded mode. To this end, we build a controller based on the power-frequency swing equation, which employs the rotor momentum of inertia and damping coefficient as control parameters to mimic the characteristics of the synchronous generators.

CHAPTER 2

LITERATURE REVIEWS

A large number of approaches to emulate synchronous generator characteristics have been proposed and developed. Despite utilizing an identical fundamental concept, they vary with dissimilarities in terminology, targeted applications, and suggested control algorithms [13]. An overall categorization of numerous topologies is illustrated in Figure 2.1. The synchronous generator model-based approach applies a full mathematical model of the synchronous generators to model the exact behaviors of their dynamics. Another approach attempts to propose a less bulky dynamic model to approximate the behavior of synchronous generators by examining only the swing equation, while the frequency-power response based topology focuses on the characteristics of frequency deviation response of the synchronous generators [12]. Each technique, depending on the design purposes and the degree of sophistication, has its pros and cons. Some of the existing representatives for each approach will be reviewed and compared in more detail by evaluating their key features and weaknesses.

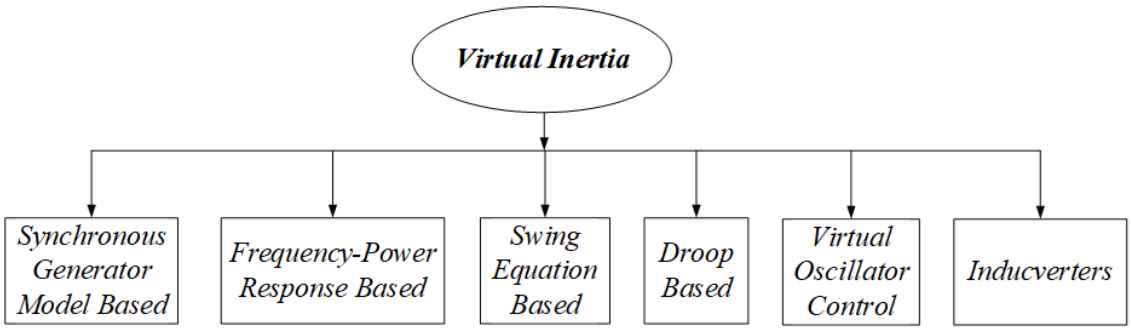

Figure 2.1: Classification of Different Virtual Inertia Approaches

Regarding the synchronous generator model-based approach, VISMA can be referred to as the first power electronics-based approach of making renewable electric generators mimic the electromechanical synchronous machines. VISMA, initialized by Beck and Hesse in 2007, is based on the dq-frame reference rotational frame to derive the syn-

chronous generator's mathematical model [14, 15]. Stator currents of the virtual machine are calculated and injected through a hysteresis current control approach. However, instability due to the mathematical divergence of Euler's method and the impact of digital signal processing architecture on numerical representation are limitations of this approach [12]. To improve robustness, a simplified three-phase model, which provides the features of virtual mass and virtual damping according to the electromechanical power balance, was rebuilt [16]. A pole wheel induction voltage replaces the field circuit in the stator, and the damping attribute is incorporated in the mechanical subsystem. It demonstrated that grid frequency oscillation caused by the load activity could be attenuated. The virtual mass counteracts grid frequency reduction, and the virtual damper suppresses grid oscillation. This method is especially effective under unsymmetrical load conditions or rapid disturbances in the grid. Another method employing the VISMA model as a voltage source is the Institute of Electrical Power Engineering (IEPE) Topology [17]. While VISMA utilizes the voltage as the input, the output current in the IEPE strategy is the input, and from that, reference voltages are computed and generated for the virtual model. The IEPE topology is more appropriate for the islanded mode than for the grid-imposed mode due to the complexity of transient currents during the synchronization. A concept of control based on a virtual generator model of algebraic type was formulated [18]. The utilization of an automated voltage regulator (AVR) and an equivalent governor to produce voltages and phase command is the main idea of this method. However, many issues need to be further investigated, including the control scheme, the settings of parameters, and the incorporation of the dq-frame transformation.

Synchronverter [19], meanwhile, is one of the latest common terminology representing this category. This concept permits the static interfaced distributed generators to mimic precisely the synchronous generators principles and was well developed further in 2016 [20, 21]. The electrical and mechanical components of the synchronous generators

are both examined to derive an exact mathematical model. Specifically, stator and field flux linkage equations are derived from self and mutual inductance between the field coil and three stator coils to infer the back electromotive force (emf) equation. Besides, the moment of inertia in rotating masses is based on the swing equation, which is the same underlying concept as the swing equation-based technique. However, the difference is that, the electromagnetic torque is found from the energy stored in the machine magnetic field and rotor angle. Real and reactive power are adjusted by a real power-frequency droop control loop [22]. The below equations are utilized to implement a synchronverter concept:

$$T_e = M_f i_f < i, \widetilde{sin\theta} > \tag{2.1}$$

$$e = \dot{\theta} M_f i_f \widetilde{sin\theta} \tag{2.2}$$

$$Q = -\dot{\theta} M_f i_f < i, \widetilde{cos\theta} > \tag{2.3}$$

where T_e is the electromagnetic torque of the synchronverter, M_f is the magnitude of the mutual inductance between the field coil and the stator coil, i_f is the field excitation current, θ is the angle between the rotor axis and one of the phases of the stator winding, e is no-load voltage generated, Q is the generated reactive power, $< .,. >$ denotes the inner product of two vectors in $\mathbb{R}^3$, i and $\widetilde{(.)}$ denote vectors comprising three 120^0 out-of-phase components [19]. The controller design based on Equations 2.1, 2.2 and 2.3 is modeled in Figure 2.2. The non-presence of frequency derivative terms, which produce noise in the system, is regarded as the main strength of the control design. Despite being able to build a full model of the electrical and mechanical components of the synchronous generators, the level of complication of the differential equations can lead to numerical instability. Another drawback of this strategy is the lack of current-mode control, which cannot protect the system against over-current conditions. Extra over-current protection is needed to ensure safe operation [12]. An improved synchronverter controller diagram was proposed with the added utilization of Park's transformation to implement an electromagnetic transient

module, along with a virtual governor and a rotor swing mathematical model [23].

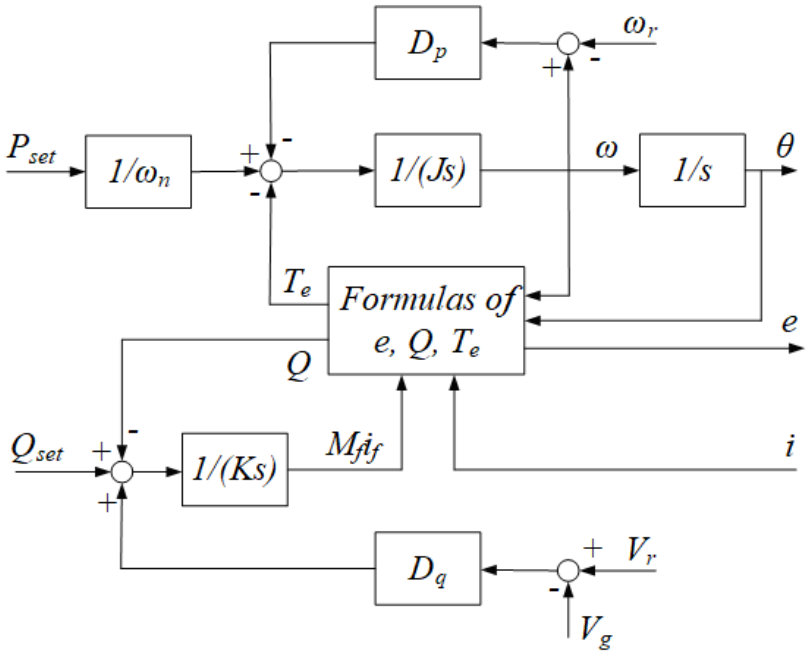

Figure 2.2: Synchronverter Controller Diagram

The initial model of the synchronverter controller utilizes a phase-locked loop (PLL) to synchronize with the grid frequency. It has a significant impact on the dynamical behaviors of the system. However, the drawbacks of a synchronization unit on the control performance [24–26] negatively affect the stability of the system and obstruct quick and accurate synchronization. Different research has been done to enhance the synchronization speed and precision of the PLL [27–29]. A self-synchronized mechanism [21], which can automatically synchronize with the grid before connection and track the grid frequency after connection without the need of a dedicated synchronization unit, was proposed. Not only for the inverters, but this control strategy was also applied to three-phase PWM rectifiers to achieve virtual inertial response from the load side [30]. Another point in the original synchronverters model is the utilization of a filter inductor, which is much smaller than a stator inductor in a conventional synchronous machine. This difference results in the dissimilarity in their behaviors and performances since a small inductor is not benefi-

cial for the system stability [31]. A method was presented to virtually enhance the filter inductor only by modifying the algorithm [32]. Not only the filter inductor-related problems, altering the dynamic response speed of the active-power loop inevitably impacts the steady-state frequency droop mechanism. Hence, an auxiliary loop, named as a damping correction loop, was added so that the active-power loop can be regulated without any restrictions [33]. A lot of attempts have been made to establish the stability of the synchronverters. The problem becomes more challenging due to the non-linear dynamics of the system. Motivated by the bounded integral controller [34], a new control strategy that guarantees given bounds for the frequency, and the voltage separately from each other was developed [35]. From a preliminary design proposal [36], the method was further developed to sustain given bounds for both the field-excitation current and the frequency. This method defines a particular bound for the synchronverter's voltage and secures the closed-loop system's asymptotic stability and the distinctiveness of a requested equilibrium point based on non-linear dynamic modeling. This approach improves the stability as there is no need for additional saturation units.

In order to simplify the mathematical model of the synchronous generators, a control strategy developed by Ise lab deals only with the swing equation and investigates the response in the presence of a grid voltage dip [37]. The swing equation is well-known from the publications on power system stability and dynamics [38] and is shown as:

$$J\frac{d\omega}{dt} = T_m - T_e - D(\omega - \omega_g) \tag{2.4}$$

where J is the rotor momentum of inertia, D is the damping coefficient accounting for the damping torque associated with the damper windings during transient conditions, ω is the rotating speed of the machine, ω_g is the angular frequency of the grid. It should be noted that the coefficient D in a real synchronous machine is not a constant number. It is contingent on the operating point of the machine. Hence, a reduced-order model with a fixed value of D cannot match the inertial behavior in the entire operating range. By multiplying

by the frequency ω, the swing equation can be expressed in terms of power. For small oscillations around the synchronous conditions, the power balance can be represented by the approximation given by Equation 2.5, where P_m is the prime mover input power [39], emulating mechanical power of the synchronous generator, P_e is the active output power, simulating electrical power of the synchronous generator, K_D is the damping constant associated with D:

$$J\omega_g \frac{d\omega}{dt} = P_m - P_e - K_D(\omega - \omega_g) \tag{2.5}$$

Typically, for a conventional synchronous generator, its moment of inertia and the damping coefficient are almost constant values. Nevertheless, due to the control purposes to obtain effective dynamic response, moment of inertia and damping factor in the virtual inertia emulation can be altered in real-time. Based on Equation 2.5, a virtual inertia controller diagram can be designed in the Laplace domain and is shown in Figure 2.3. By taking the integral of the virtual angular frequency ω, the virtual phase angle θ is generated as a phase command of the inverter output voltage and sent to the PWM generator. The voltage reference e can be produced by the $Q - V$ droop approach [40, 41]:

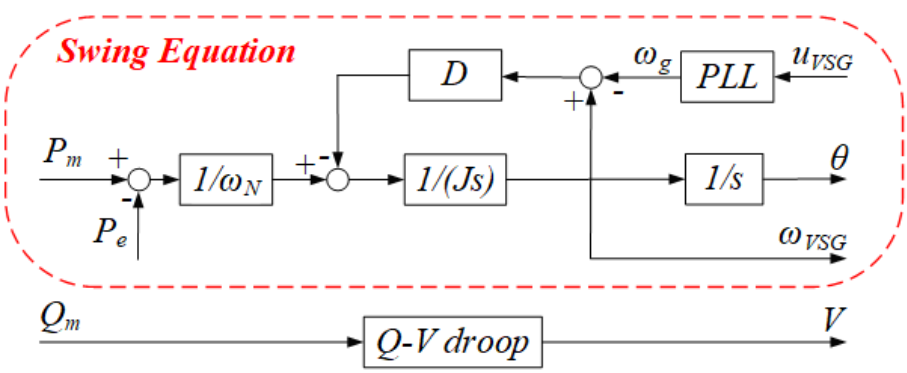

Figure 2.3: Swing Equation-Based Controller Diagram.

This strategy has the same benefit as the synchronverter's topology of not employing the frequency derivatives and can be used to function distributed generators as grid-forming

units. To mimic the frequency and voltage dynamics of an actual power network as precisely as possible, a three-phase synchronous generator model, inspired by the swing equation, is employed to simplify an ideal voltage source behind an impedance [42]. The idea of the swing equation-based controller model was applied to show an equivalent dynamics of a speed-controlled permanent-magnet synchronous generator [43]. Nevertheless, the lack of the current-mode control is still a limitation from the view of over-current protection. Another weakness of this technique is the consequences of inaccurate tuning of the moment of inertia value J and damping factor D_p, which can result in deviatory system reactance [39]. In order to protect the system under over-current conditions and improve robustness for the system, a current-control scheme based on the virtual admittance concept was proposed [44], named as synchronous power controller (SPC). The underlying dynamic equation of this concept in the Laplace domain is:

$$i(s) = \frac{1}{Rs + L}(e(s) - v(s)) \tag{2.6}$$

where v is the voltage at the point of common coupling (PCC), e is the AC internal induced electromotive force (emf), R, and L are the output impedance of the generator. The electrical characteristics in Equation 2.6 are known for better stability and less sensitivity to distortions, compared to the virtual impedance methodology. The SPC design purpose is not to mimic the response of the synchronous generator but to optimize its response in the presence of perturbations and fluctuations by offering a second-order over-damped response to the system. The SPC can be integrated into conventional PV systems without modifying the structure of the hardware. Some advantages of this strategy are the ability to switch modes between islanded and grid-connected mode flexibly without triggering any unwanted transients and secure a complete range of harmonic frequencies and the simplicity in the inner loop implementation [45]. Based on the idea of the SPC, a power-loop controller was proposed to configure damping and flexible droop characteristics separately to support the frequency [46]. The power loop controller sets up damping and droop charac-

teristics independently, without tuning a single parameter to find a good trade-off between damping and droop characteristics. The power control loop is in the form of:

$$G_{PLC}(s) = \frac{K_P s + K_I}{s + K_G} \tag{2.7}$$

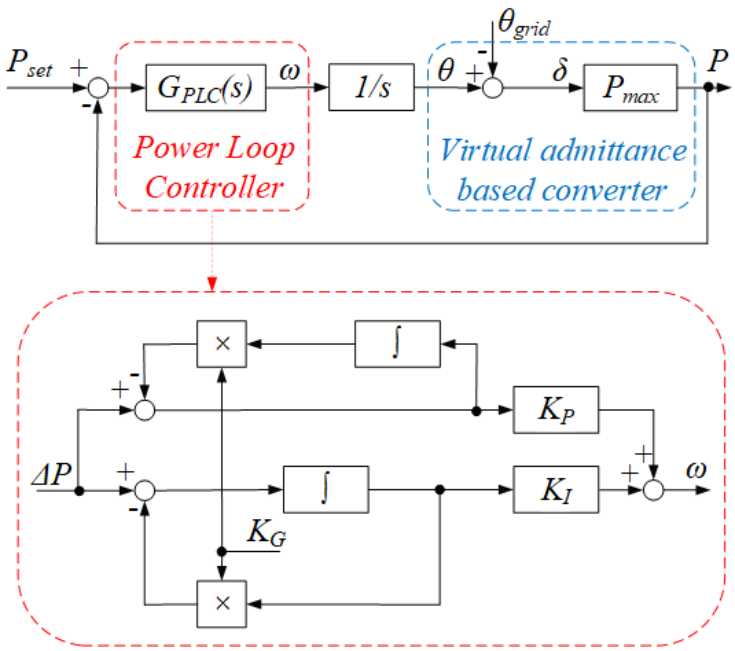

Figure 2.4: Power Control Loop Diagram with Virtual Admittance.

The proposed model demonstrated its flexibility in comparison with the existing virtual inertia methodology. The model can prevent the constraint between the damping and droop characteristics in the power regulating loop [46]. A comparison of various power-loop controllers was discussed [47]. Another concern in this topology is that power oscillation with high amplitude after a disturbance may shut down the operation due to low transient condition tolerance of the virtual model. An alternating inertia control was proposed to remove the oscillation [39], thus enhance the reliability of the system. The paper demonstrated the effectiveness of the proposed controller, which can regulate the values of the moment of inertia J and damping factors D flexibly to suit each scenario of power oscillation. This strategy does not only enhance the stability, but also suppresses the frequency

and power oscillations effectively. Inspired by the same method of the virtual stator reactance [32], the swing equation-based control strategy guarantees accurate reactive power sharing even if there are line impedance mismatch and active power sharing changes [48]. To obtain a smoother transition after a significant disturbance, an algorithm, named as particle swarm optimization (PSO) [49], was implemented into the swing equation-based model to find the optimum values of the moment of inertia and damping factor. The results showed that it could maintain the integrity by ensuring the voltage angle deviation of generators inside the limit in fault conditions, but under heavy load status, the transient stability is still a challenge [50].

As one of the simplest topology, the power-frequency response-based topology utilizes the derivative of frequency measurement to emulate the absorption or release of kinetic energy during frequency deviation to improve the inertial response to rotor speed deviation performance. A typical control strategy in this group is the virtual synchronous generator (VSG) [51–53]. While the traditional droop loop only allows frequency alteration, the ability to control dynamic frequency is noticeable in this approach [54]. Equation 2.8 shows the basic underlying concept of this strategy:

$$P = K_D \Delta\omega + K_I \frac{d\Delta\omega}{dt} \tag{2.8}$$

where P is the output power, K_D and K_I are the damping, and inertial gains, $\Delta\omega$ and $\frac{d\Delta\omega}{dt}$ are the changes in angular frequency and ROCOF, respectively. The frequency derivative allows a fast dynamic frequency response, which captures the ROCOF. Its output is adjusted depending on the frequency variations, representing the generator as a current source. The controller includes a mathematical model of Equation 2.8, a PLL, and a current-mode controller, which offers over-current protection for the system [55]. For current-mode control in the dq-frame, d-axis current reference can be computed as:

$$I_d = \frac{2}{3}\left(\frac{V_d P - V_q Q}{V_d^2 + V_q^2}\right) \tag{2.9}$$

where V_d and V_q are d- and q-axis voltage components at the PCC. The q-axis component of the current I_q is set to 0 as it is active power control. The current-control diagram based on Equations 2.8 and 2.9 is described in Figure 2.5 [55]:

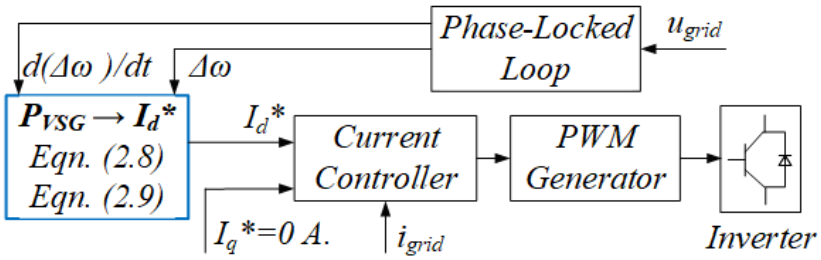

Figure 2.5: Virtual Synchronous Generator Control Diagram.

This strategy has been proved beneficial for further research through a laboratory test-setup in real-time simulation using power hardware-in-the-loop (PHIL) [56]. The results showed that the VSG model could reduce the size of frequency deviations originated by load alterations. The steady-state error of frequency experienced a decline of 35%, and a decrease of 58% in the dynamic frequency error could be achieved before settling to a steady state. Additional reductions of 13% and 14%, respectively, can be achieved by changing the algorithm's constants. VSG was also applied in the inverter-based system of wind energy [6, 57]. Regardless of many excellent features, it must be remarked that this methodology is only trying to model the inertia effect with respect to the response to ROCOF, together with a steady-state power droop, and does not aim to design an internal mathematical model of the machine inertia. Hence, the presence of an external voltage with a physical inertia is required to implement the virtual inertia by Equation 2.8 [13]. This topology is only suited for a grid-connected system where the system does not have to work as a grid forming unit. Furthermore, instability can be caused by various units of operation [58].

Another limitation is the lack of implementation for the input power alteration process [46], the challenge to deal with the instability of the PLL, and the frequency deriva-

tive's sensitivity [11, 59]. The use of a proportion-integral (PI) controller for the inner current-control loop is also known for instability [60]. In order for the system to cope with considerable power changes, an approximate dynamic programming (ADP) methodology was proposed for online parameter tuning of the proportional-derivative (PD) virtual inertia control [61]. With this method, the frequency does not drop too low while still securing the rotor speed in a permissible range. The algorithm can help the system adapt to new conditions through learning to generate the most efficient parameters automatically. A more efficient self-tuning methodology, which can regulate its inertia and damping factor when needed, was proposed [62]. This methodology offers a better control the frequency excursions while declining the settling times and the energy used from the energy storage system (ESS). Its inertial response and damping powers were evaluated and compared with the ones of constant-parameters VSM in different scenarios. It was demonstrated to perform similarly but to obtain a significant energy efficiency and a reduction in power flow of 58%. Furthermore, less energy was consumed per frequency unit, which proved a more efficient frequency attenuation. Instead of using a proportional-integrative-derivative (PID) controller due to the inability to adapt to alteration in operating conditions, supplementary adaptive dynamic programming controllers with online learning control were used to enhance the dynamics of virtual inertia [63]. This controller stabilizes the system frequency faster, which reduces the time for supplying energy as well as energy consumption from ESS. The method proves its efficiency of 33.78% reduction in total energy consumption compared with the conventional VSM, thus reduces the cost of sizing ESS and the running cost of VSM. The transient peak power generated by this enhanced controller is also lower than the original VSM, which lowers the cost of filters and power switches. Implementing virtual inertia to the system can extend the frequency settling time, resulting in enhanced energy exchange from the ESS, which remarkably reduces the life of the ESS. This supplementary ADP using a neural network structure efficiently reduces the settling time from

44.75 seconds to 38.01 seconds.

Different from the above techniques, another study adopting frequency and voltage droops indicates a considerable improvement in microgrid dynamic behavior in islanded-mode [64]. The principles of the frequency and voltage droop were explained that, as two operating units share both active and reactive loads, the loops help avoid circulating currents [65]. This approach is also implemented with a frequency restoration algorithm that moves the droop characteristics in the vertical direction at a rate proportional to the power rating. This allows frequency restoration while sustaining the power-sharing [66].

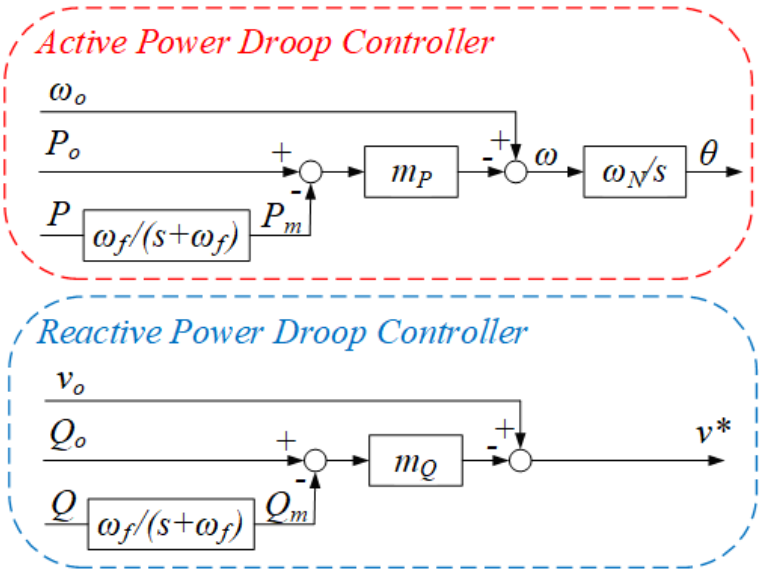

Figure 2.6: Frequency Droop Controller Diagram.

Also, the utilization of a low pass filter for the measured active power at the grid interface has been proved to stabilize the control loop in this strategy [67]. The inertial responses of this more straightforward droop-based approach and the more complex VSM topology have been demonstrated almost equivalent through numerical simulations [68]. Despite some good features, drawbacks of the droop include slow transient response, a trade-off between power-sharing precision and voltage oscillation, unbalanced harmonic current sharing, and a high dependency on the inverter output impedance [69]. Several

methods tried to modify the droop model to overcome the pre-mentioned problems [70–72], while an adjustable virtual impedance topology was proposed [73]. An essential advantage of employing a virtual output impedance is that the magnitude and phase angle of the output impedance can be controllable variables. However, the excessive dependency on the voltage loop bandwidth appears to be a limitation of this implementation [74]. An inertial droop control was proposed through the comparison of dynamic characteristics between the VSG and the droop control [75]. By doing some experiments, the similarity between the two methods is the active power controls of both VSG control and droop control are stable. However, it was found that the delay in the active power droop controller of the droop control can enhance the inertia, while the delay in the governor of the VSG model lowers the inertia and amplifies oscillation. Thus, the governor delay is recommended to be removed. Another point is that a well-designed first-order lead-lag unit in the active power droop controller has a similar small-signal model to that of the VSG control, which can be modified to obtain a novel inertial droop control. The new proposed controller design inherits the advantages of both methodologies.

Another new technique, inspired by induction motor working principles, was proposed in 2016 [59]. This control proposal, named as inducverters, eliminates the need for a dedicated synchronization process and resembles the characteristics of an induction machine. It originates from the idea that the induction machine has self- and soft-start capability and automatic synchronization mechanism, and can track its variations without any feedback from the grid. In comparison with the synchronverters where any variations in the grid frequency can lead to a permanent offset of output powers, real and reactive power outputs of the inducverters are continuously fed regardless of the changes in grid parameters. On the other hand, another approach did not focus on building the inertial model of the generators. Instead, it tried to simulate a non-linear dead-zone oscillator's dynamics, which was named as a virtual oscillator control strategy [76, 77]. This approach can control the inverters

without communication and can be applied to both linear and non-linear loads [76]. Small errors in the virtual oscillator parameters are known for bounded voltage synchronization errors [78]. Hence, the publication proposed a parameter selection methodology that the inverter terminal voltages oscillate at the desired frequency, and the load voltage is kept between the set upper and lower bounds.

Finding an effective way to integrate distributed energy resources using virtual inertia concept into a real large-scale grid is one of the hardest challenges in the future. A methodology was proposed using a modified frequency regulation improved from the previous VSM works, a dual droop control, and a power system stabilizer to increase the system stability [79]. The results showed that the dynamics of the AC output became independent; the system could obtain the power balancing and sharing with the grid under various conditions and generate any output power in steady-state. Thus, it was verified to be a smart and autonomous approach to integrate a higher penetration level of DERs into the grid. Another concern lies in the energy consumption of data centers, composed of energy infrastructure such as PV solar, natural gas generators, and uninterruptible power supplies (UPS) in the form of batteries. The data centers were explained that they could operate as virtual power plants [80]. An energy management system to operate the data centers as a virtual power plant was proposed in order to obtain considerable energy saving for energy infrastructure [80, 81]. Not only beneficial for data centers; in particular, the management also provides reliability and economic efficiency. While most published research is about virtual inertia implementation, mathematical models of system dynamics are still needed to support parameter tuning processes and understanding of operational behavior between the grid and the virtual inertia system. A linearized small-signal model of the VSM in islanded mode has been developed [82]. The model has been verified to generate the same simulation results as the model with nonlinearities. The linearized model has been utilized to analyze and evaluate the system eigenvalues and their sensitivities to the parameter gains.

On the other hand, some research tries to assess the economic benefits of inertia response provision. A methodology was developed to incorporate both inertia of conventional generators and synthetic inertia provided by wind plants into the system scheduling [83]. Thus, it supports the cost-benefit analysis to determine the optimal amount of wind plants to be equipped with virtual inertia capability. The virtual inertia of wind plants are added to the total system inertia by estimating the online capacity of wind plants as a function of system-wise generation. The results suggested that the operation cost could be reduced by the virtual inertia with high penetration of wind generation. Nevertheless, the benefits of further improvement become limited as soon as the synthetic inertia constant reaches 3s. It was shown that after some threshold, only provide virtual inertia could not reduce the system operation cost any more.

To sum up, a comparison of different pre-mentioned virtual inertia methodologies is summarized in Table 2.1 [12]:

Table 2.1: Comparison of Different Virtual Inertia Methodologies

Methodology	**Key features**	**Limitations**
Synchronous Generator (SG) model-based	• Exact replication of SG dynamics • No need of frequency derivative • Phase locked loop (PLL) utilized only for synchronization	• Numerical instability concerns • Typical implementation for voltage-source mode; lack of over-current protection
Swing Equation based	• Simpler mathematical model in comparison with SG based model • No need of frequency derivative • PLL utilized only for synchronization	• Frequency and power oscillations • Typical implementation for voltage-source mode; lack of over-current protection
Frequency-Power Response based	• Straightforward implementation • Typical implementation for current-source mode; inherent over-current protection	• Instability caused by PLL, particularly in weak grids • Susceptible to noise due to the utilization of frequency derivative
Droop-based approach	• Elimination of PLL • Resemble the traditional droop control concept in SGs	• Slow transient response • Inaccurate transient active power sharing
Virtual Oscillator Control	• Elimination of PLL • Emulate the dynamics of a nonlinear dead-zone oscillator	• Bounded voltage synchronization errors caused by errors in the model parameters
Inducverters	• Elimination of PLL • Mimic induction machine characteristics	The concept is still at its early stage and needs more investigation and evaluation.

CHAPTER 3

THEORETICAL BACKGROUND AND CONTROL DESIGN

This chapter presents the analysis technique and control design methodology of a voltage-source inverter with the swing equation-based virtual inertia implementation under grid-connected and islanded mode. It includes fundamentals of sinusoidal pulse-width modulation (SPWM), direct-quadrature-zero (dq0) transformation, phase-locked loop (PLL), current-mode control and real-/reactive-power controller of grid-imposed frequency voltage-source converter (VSC) system, voltage and frequency control of controlled-frequency VSC system, and virtual inertia controller design based on swing equation.

3.1 VOLTAGE-SOURCE INVERTER

Inverter is a power electronic (or static) converter that converts a DC power supply into an AC output of the desired manner, according to pre-specified performance specifications. Depending on the source at the DC side of the inverters, they are classified as either voltage-source inverter (VSI) or current-source inverter (CSI). If the DC input is a voltage source, then the inverter is named a VSI. A relatively large DC link capacitor feeds the power input of a VSI in order to maintain the magnitude of the voltage constant. Based on the number of phases, inverters are categorized into two types: single-phase inverter and three-phase inverter.

Characteristics of a static converter are primarily contingent on the kind of its semiconductor switches, classified as: uncontrollable, semi-controllable, and fully controllable switches. In this research, the fully controllable switches, whose gating command can determine conduction and interruption instants, are utilized. Almost conventional fully controllable switches are composed of metal-oxide-semiconductor field-effect transistor (MOSFET), insulated-gate bipolar transistor (IGBT), gate-turn-off thyristor (GTO) and integrated gate-commutated thyristor (IGCT).

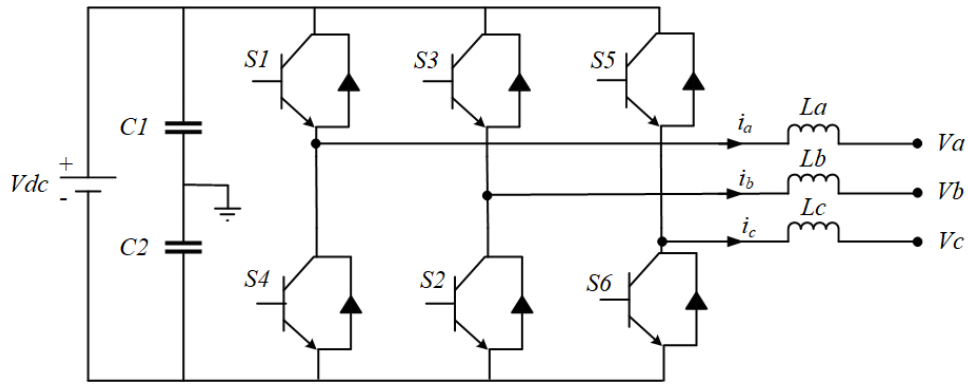

Figure 3.1: Three-Phase Voltage-Source Inverter.

3.2 Sinusoidal Pulse-Width-Modulation Technique

Pulse-width-modulation (PWM) technique is the most common and efficient control method within the power electronic converters. PWM techniques are identified by constant rectangular amplitude pulses with different duty cycles for each period. The pulses width is modulated to secure the inverter average output voltage and to eliminate its harmonic content by turning the switch between supply and load at a fast rate. This process results in the variation of the average value of the waveform. The lengthier the on-switch duration is compared to the off periods, the more the total power is supplied to the load.

There are various PWM techniques, classified into two categories comprising fundamental switching frequency and high switching frequency PWM. Sinusoidal pulse-width-modulation (SPWM), one of the most common PWM techniques in industrial applications, belongs to the high switching frequency category. In SPWM, the pulses width over the output cycles is modified in a sinusoidal manner. Its basic principle is based on the comparison of a high-frequency triangular carrier voltage with a sinusoidal modulating signal representing the desired fundamental component of AC output. Working principle of the SPWM is demonstrated in Figure 3.2 [84]. A modulating signal (v_m) with a desired voltage output is compared with the carrier signal (triangular waveform v_c). If $v_m > v_c$, the gating signal is ON and vice versa. The frequency of the carrier signal determines the switching

frequency of the inverter. The amplitude and the frequency modulation ratio of SPWM are defined as the ratio of the modulating signal's peak over the carrier signal's peak, and the ratio of the modulating signal frequency over the carrier signal frequency, respectively. The inverter's output voltage is altered by changing the magnitude of the modulating signal while keeping the magnitude of the carrier signal fixed. For the three-phase PWM inverter, to achieve symmetrical three-phase output voltages, three sinusoidal voltages with an identical magnitude but 120^0 out of phase are measured with the same triangular waveform.

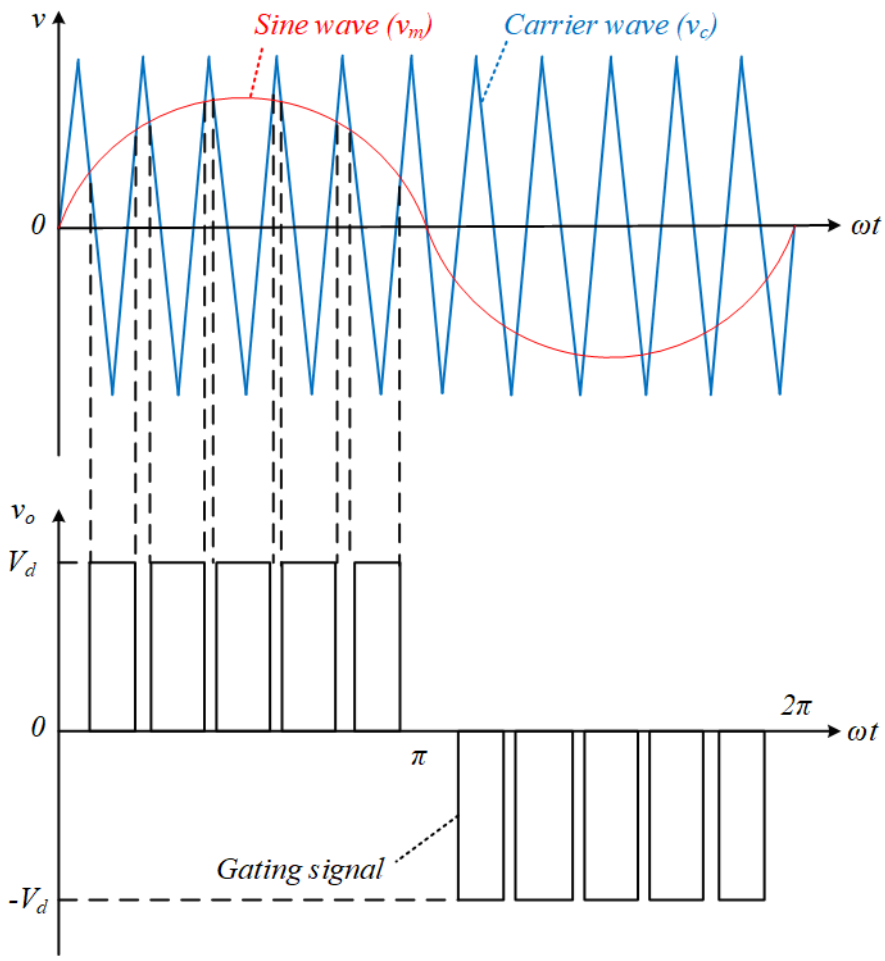

Figure 3.2: Sinusoidal Pulse-Width Modulation Mechanism.

3.3 Space Phasor and dq-Frame Representation

In order to simplify the analysis and control in the VSC system, Clarke's ($\alpha\beta$) and Park's (dq) transformation are introduced to solve equations exhibiting time-varying quantities, mutually coupled inductances. By referring all variables to one reference frame, the mathematical model of the system becomes less complicated, and it is easier to design the controller. The $\alpha\beta$-frame and the dq-frame are also named as the stationary and the rotating frame.

Space phasor is firstly presented as a core concept of the two-dimensional reference frames. Symmetrical three phases can be represented by a set of space-phasor equations:

$$\vec{f}(t) = \left(\hat{f}e^{j\theta_0}\right)e^{j\omega t} = \frac{2}{3}\left[e^{j0}f_a(t) + e^{j\frac{2\pi}{3}}f_b(t) + e^{j\frac{4\pi}{3}}f_c(t)\right], \tag{3.1}$$

where $\hat{f}$, θ_0, ω are the amplitude, the initial phase angle, and the angular frequency of the function, respectively [84].

Real, reactive, and apparent power in space phasor theory can be expressed as:

$$P(t) = Re\left\{\frac{3}{2}\vec{v}(t)\vec{i}^*(t)\right\} \tag{3.2}$$

$$Q(t) = Im\left\{\frac{3}{2}\vec{v}(t)\vec{i}^*(t)\right\} \tag{3.3}$$

$$S(t) = P(t) + jQ(t) = \frac{3}{2}\vec{v}(t)\vec{i}^*(t) \tag{3.4}$$

Conventionally, a complex-valued function of time can be represented in the polar coordinate system. For control design and implementation purposes, space phasors and space-phasor equations are represented in the Cartesian coordinate system where real-valued functions of time are in presence. In space-phasor domain, an asymmetrical three-phase is not able to be directly represented. Hence, the mapping of a space phasor onto the Cartesian coordinate system is introduced in Figure 3.3 [84], which is commonly referred to as Clarke's transformation.

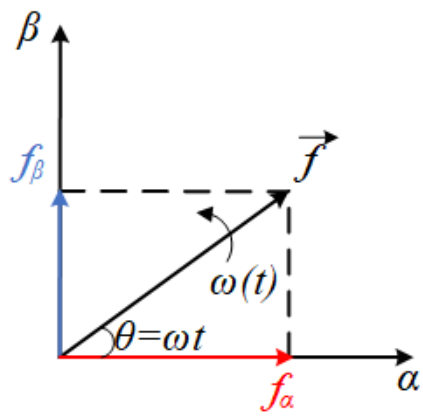

Figure 3.3: Clarke's Transformation.

The Clarke's transformation converts the time-domain components of a three-phase system in an abc reference frame into components in a time-varying orthogonal stationery $\alpha\beta$ frame. The space phasor vector $\vec{f}$ can be decomposed into its real and imaginary components as:

$$\vec{f}(t) = \left|\vec{f}\right| \angle\theta = f_\alpha(t) + jf_\beta(t) \tag{3.5}$$

where:

$$\left|\vec{f}\right| = \sqrt{f_\alpha^2 + f_\beta^2}\theta = tan^{-1}\left(\frac{f_\beta}{f_\alpha}\right) \tag{3.6}$$

It can be deduced by equating the corresponding real and imaginary parts of both sides of the resultant:

$$\begin{bmatrix} f_\alpha(t) \\ f_\beta(t) \end{bmatrix} = \frac{2}{3}\begin{bmatrix} 1 & -\frac{1}{2} & -\frac{1}{2} \\ 0 & \frac{\sqrt{3}}{2} & \frac{-\sqrt{3}}{2} \end{bmatrix}\begin{bmatrix} f_a(t) \\ f_b(t) \\ f_c(t) \end{bmatrix} \tag{3.7}$$

Power expression in the Clarke's transformation in terms of $\alpha\beta$-frame variables can be obtained by substituting $\vec{v}(t)$ and $)\vec{i}^*(t)$ into Equations 3.2 and 3.3:

$$P(t) = \frac{3}{2}\left[v_\alpha(t)i_\alpha(t) + v_\beta(t)i_\beta(t)\right] \tag{3.8}$$

$$Q(t) = \frac{3}{2}\left[-v_\alpha(t)i_\beta(t) + v_\beta(t)i_\alpha(t)\right] \tag{3.9}$$

In the Clarke's transformation, the signals are in general sinusoidal functions of time, making the controller design still not a straightforward task. Therefore, Park's transformation, in which signals become time-invariant, is introduced to allow the utilization of compensators with simpler structures, smaller dynamic orders, and zero steady-state tracking error [84]. The Park's transformation, shown in Figure 3.4 [84], converts the time-domain components of a three-phase system to direct, quadrature, and zero components in a rotating reference frame. For a balanced system, the zero component is equal to zero. The Park's transformation is an implementation of the Clarke's transformation, in which the orthogonal quantities achieved from the Clarke's transformation are combined with a rotating component to turn it into a rotating frame. The $\alpha\beta$ to dq-frame transformation is defined by:

$$f_d + jf_q = (f_\alpha + jf_\beta)e^{-\varepsilon t} \tag{3.10}$$

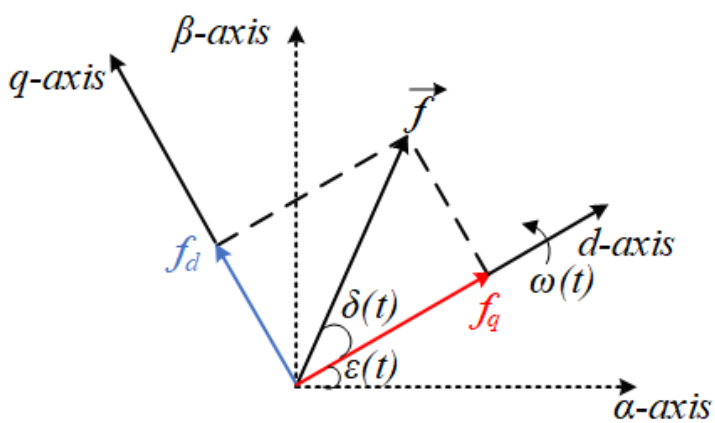

Figure 3.4: Park's Transformation.

The relation between the abc and the dq-frame transformation is described as:

$$\begin{bmatrix} f_d \\ f_q \\ f_0 \end{bmatrix} = \frac{2}{3} \begin{bmatrix} cos[\varepsilon(t)] & cos[\varepsilon(t) - \frac{2\pi}{3}] & cos[\varepsilon(t) - \frac{4\pi}{3}] \\ sin[\varepsilon(t)] & sin[\varepsilon(t) - \frac{2\pi}{3}] & sin[\varepsilon(t) - \frac{4\pi}{3}] \\ \frac{1}{2} & \frac{1}{2} & \frac{1}{2} \end{bmatrix} \begin{bmatrix} f_a \\ f_b \\ f_c \end{bmatrix} \tag{3.11}$$

The formulations of real and reactive power in terms of dq-frame variables are derived by substituting $\vec{v}(t)$ and $\vec{i}^*(t)$ into Equations 3.2 and 3.3:

$$P(t) = \frac{3}{2}\left[v_d(t)i_d(t) + v_q(t)i_q(t)\right] \tag{3.12}$$

$$Q(t) = \frac{3}{2}\left[-v_d(t)i_d(t) + v_q(t)i_q(t)\right] \tag{3.13}$$

where i_d and i_q are d- and q-axis components of current, respectively.

If the synchronous rotating frame in Figure 3.4 is equal in phase with the space phasor vector $\vec{f}$, then the d-axis component is equal to the magnitude of the voltage, and the q-axis component becomes 0. In case $v_q = 0$, it can be noticed that the real and reactive power can be proportional to i_d and i_q, respectively, as well as independently controlled [84]. This property is commonly utilized in the control of grid-connected three-phase VSC systems mentioned in later sessions.

3.4 Phase-Locked Loop

A phase-locked loop (PLL) is a controller that generates an output signal whose phase is associated with the phase of an input signal by comparing the phase of a reference signal to the phase of an adjustable feedback signal. It utilizes a negative feedback control loop operating in the frequency domain with a voltage-controlled oscillator (VCO), whose operating frequency is controlled by a voltage. The comparison generates pulses whose duration is the time from the input edge to the oscillator edge and sends the pulses to a low-pass filter. The output of the filter is the control voltage to the oscillator. When the output frequency and phase are matched to the incoming frequency and phase of the error detector in steady-state, the PLL is locked. The basic block diagram of the PLL is shown in Figure 3.5 [85]:

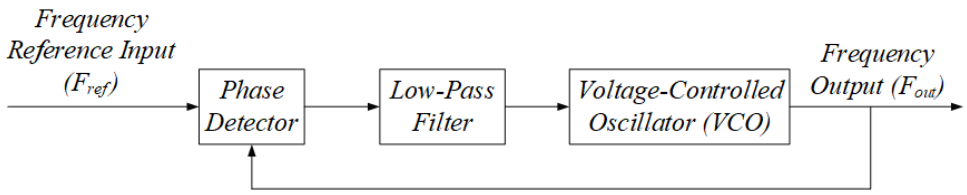

Figure 3.5: Phase-Locked Loop Diagram.

In a grid-connected VSC system examined in the dq-frame, the PLL approximates and delivers the angle of the grid voltage imposed on the VSC by the grid. It acts as a synchronization mechanism and is needed in the dq-frame control. However, the PLL is regarded as a demerit in the dq-frame control due to the instability of its dynamics. Further implementations have been developed to improve the dynamics of PLL [84].

3.5 Control of Grid-Imposed Frequency VSC System in dq-Frame

Grid-Imposed (or grid-connected) VSC system is a class of VSC system, in which the operating frequency is imposed by the grid. It is modeled as a DC source, an equivalent DC link capacitor, a three-phase inverter. The grid is interfaced with each phase of the VSC via a series RL branch (representing a filter) and exchanges real and reactive power with the VSC system at the PCC [84].

3.5.1 Real-/Reactive-Power Controller

In the grid-connected VSC system, the objective is to control real and reactive power the VSC system exchanges with the grid. There are two main methods for this controlling purpose; they are voltage-mode control and current-mode control. Among them, the current-mode control is more advantageous than the voltage-mode one mainly due to the ability to control line current with respect to the PCC voltage, from that to protect the system against over-current conditions [84]. Principle of current-mode control is described through a schematic diagram in Figure 3.6:

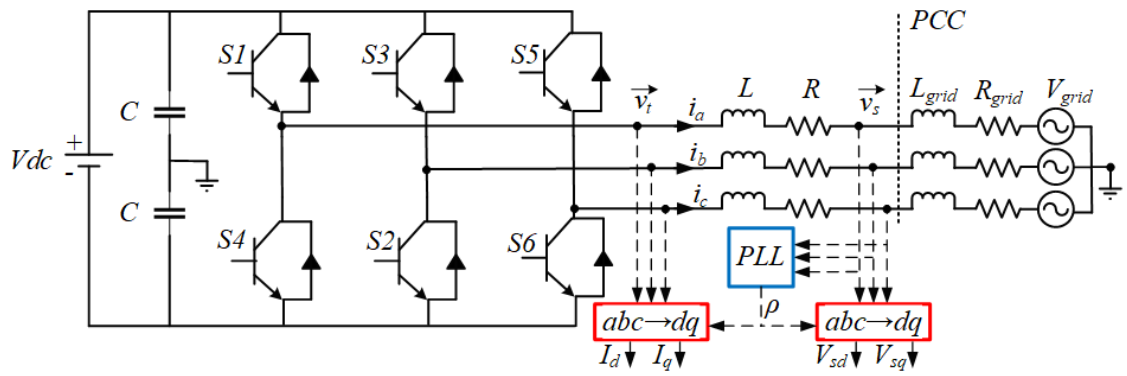

Figure 3.6: Grid-Imposed VSC System.

As can be seen, the voltage signals at the PCC are converted into the dq-frame to obtain V_{sd} and V_{sq}, which then are passed through a reference signal generator with real and reactive power references to compute and produce current references i_{dref} and i_{qref} in the dq-frame. These current references and feedback signals at VSC output terminal in the dq-frame, i_d and i_q, will be processed by compensators to generate control signals m_d and m_q in the dq-frame. These control signals are finally transformed into the abc frame and sent to the converter switches.

3.5.2 Dynamic Model of Real-/Reactive-Power Controller

From Figure 3.6, dynamics of the AC side can be expressed by the following space phasor equation:

$$L\frac{d\vec{i}}{dt} = -R\vec{i} + \vec{V_t} - \vec{V_s} \tag{3.14}$$

In the dq-frame, $\vec{i} = i_{dq}e^{j\rho}$ and $\vec{V_t} = V_{tdq}e^{j\rho}$. This inverse transformation is applied to the dynamic Equation 3.14 of the AC side. What can be deduced by splitting the resultant into real and imaginary parts is:

$$L\frac{di_d}{dt} = L\omega(t)i_q - Ri_d + V_{td} - V_{sd} \tag{3.15}$$

$$L\frac{di_q}{dt} = L\omega(t)i_d - Ri_q + V_{tq} - V_{sq} \tag{3.16}$$

where i_d and i_q are the state variables, V_{td} and V_{tq} are the control inputs, and V_{sd} and V_{sq} are the disturbance inputs.

Based on the principle of VSC control in the dq-frame, the relation between the control inputs V_{td}, V_{tq} and the modulating signals in the dq-frame m_d, m_q are:

$$V_{td}(t) = \frac{V_{DC}}{2} m_d(t) \tag{3.17}$$

$$V_{tq}(t) = \frac{V_{DC}}{2} m_q(t) \tag{3.18}$$

It can be demonstrated that the dynamics of i_d and i_q are coupled due to the $L\omega(t)$ component. To decouple the dynamics [84], two new control inputs can be assumed as u_d and u_q, then two modulating signals m_d and m_q can be set as:

$$m_d = \frac{2}{V_{DC}}(u_d - L\omega(t)i_q + V_{sd}) \tag{3.19}$$

$$m_q = \frac{2}{V_{DC}}(u_q + L\omega(t)i_q + V_{sq}) \tag{3.20}$$

Substituting V_{td} and V_{tq} into Equations 3.15 and 3.16, it can be deduced as:

$$L\frac{di_d}{dt} = -Ri_d + u_d \tag{3.21}$$

$$L\frac{di_q}{dt} = -Ri_q + u_q \tag{3.22}$$

Equations 3.21 and 3.22 show that, with the assumption of the new control inputs, the dynamics have been decoupled. i_d and i_q can be controlled by u_d and u_q, independently and respectively. From Equations 3.21 and 3.22, a control block diagram of the current-controller in the dq-frame is modeled in the Laplace domain and shown in Figure 3.7 [84]:

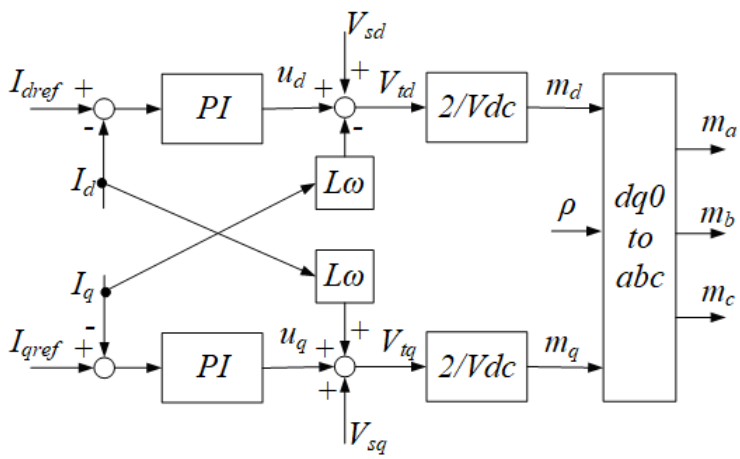

Figure 3.7: Current-Controlled Block Diagram .

The d-axis modulating signal m_d is generated based on Equation 3.21, with the contribution of u_d produced by d-axis compensator by computing and processing the error between the reference signal i_{dref} and the measured current signal i_d at the PCC. Analogously, the q-axis modulating signal m_q is generated based on Equation 3.22, with the contribution of u_q produced by d-axis compensator by computing and processing the error between the reference signal i_{qref} and the measured current signal i_q at the PCC.

An advantage offered by the dq-frame transformation is the simplicity of the compensators to track the reference signals. As all the control, feed-forward and feedback signals in the dq-frame are DC quantities in the steady-state, the compensator can be a straightforward proportional-integral (PI) controller to track a DC signal. The PI controller $k(s)$ [84] can be a simple transfer function in the Laplace domain of:

$$k(s) = k_d(s) = k_q(s) = \frac{k_p s + k_i}{s} \tag{3.23}$$

where k_p, and k_i are the proportional and integral gain, respectively. Figure 3.8 shows an equivalent current-control loop:

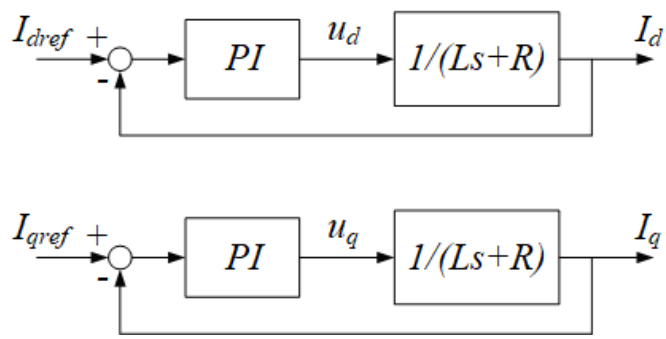

Figure 3.8: Equivalent Current-Controlled Block Diagram.

Hence, the open loop gain G(s) in the Laplace domain is:

$$G(s) = \left(\frac{k_p}{Ls}\right)\frac{s + k_i/k_p}{s + R/L} \tag{3.24}$$

This function has a pole at $s = -R/L$, which is relatively in proximity to the origin. Therefore, the zero $s = -k_i/k_p$ can cancel this pole, which simplifies the open-loop gain into $G(s) = k_p/(Ls)$. Hence, the final closed-loop transfer function is:

$$T(s) = \frac{I_d(s)}{I_{dref}(s)} = \frac{G(s)}{1 + G(s)} = \frac{1}{\tau_i s + 1} \tag{3.25}$$

where τ_i is the time constant of the resultant closed-loop system and:

$$k_p = L/\tau i \tag{3.26}$$

$$k_i = R/\tau i \tag{3.27}$$

It is pointed out that, the time constant τ_i of the first-order closed-loop transfer function, which is a design option and determines the values of proportional (k_p) and integral (k_i) gain, should be small for a fast current-control response but sufficiently considerable such that the bandwidth of the closed-loop control system $1/\tau_i$ is remarkably smaller than the switching frequency of the VSC. The time constant τ_i is normally ranging from 0.5-5 ms, being contingent on specific requirements and converter switching frequency [84].

3.5.3 Current-Mode Control of Real-/Reactive-Power Controller

From Equations 3.12 and 3.13, the real and reactive power exchanged with the AC grid at the PCC are:

$$P_s(t) = \frac{3}{2}\left[V_{sd}(t)i_d(t) + V_{sq}(t)i_q(t)\right] \tag{3.28}$$

$$Q_s(t) = \frac{3}{2}\left[-V_{sd}(t)i_d(t) + V_{sq}(t)i_q(t)\right] \tag{3.29}$$

where V_{sd} and V_{sq} are imposed by the AC grid and cannot be controlled. If the PLL is in the steady-state, $v_{sq} = 0$. Real and reactive power in the dq-frame are simplified as:

$$P_s(t) = \frac{3}{2}V_{sd}(t)i_d(t) \tag{3.30}$$

$$Q_s(t) = -\frac{3}{2}V_{sd}(t)i_d(t) \tag{3.31}$$

If the compensators can provide fast reference tracking, the real and reactive power of VSC can be controlled independently by their reference commands. As V_{sd} and V_{sq} are constants in the dq-frame, the reference tracking signals are also constants if the reference commands are constants. From Equations 3.30 and 3.31, the current-mode control can be rewritten in terms of power reference signals:

$$i_{dref} = \frac{2}{3V_{sd}}P_{sref} \tag{3.32}$$

$$i_{qref} = -\frac{2}{3V_{sd}}Q_{sref} \tag{3.33}$$

From all of the analysis, the controller design diagram for grid-imposed frequency VSC system is proposed in Figure 3.9 [84]:

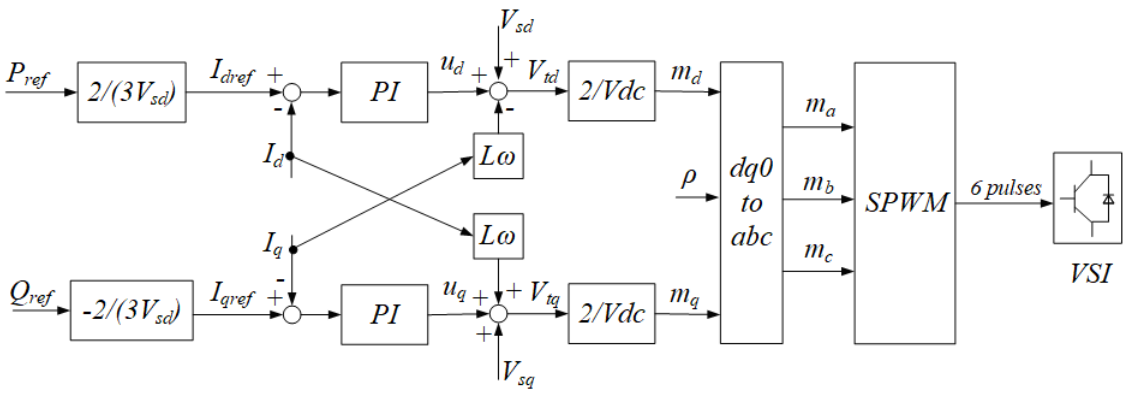

Figure 3.9: Current-Controlled Real/Reactive Power Controller Block Diagram.

3.6 Control of Controlled-Frequency VSC System in dq-Frame

Unlike the grid-connected VSC system in which the grid imposes the operating frequency, the voltage and frequency at the PCC in controlled-frequency (also called islanded) are controlled by the VSC system itself. The only difference in the configuration of controlled-frequency is, the grid is replaced by a three-phase load interfacing with the AC-side of the VSC via an RLC filter comprising a series RL branch and a shunt capacitor C_f:

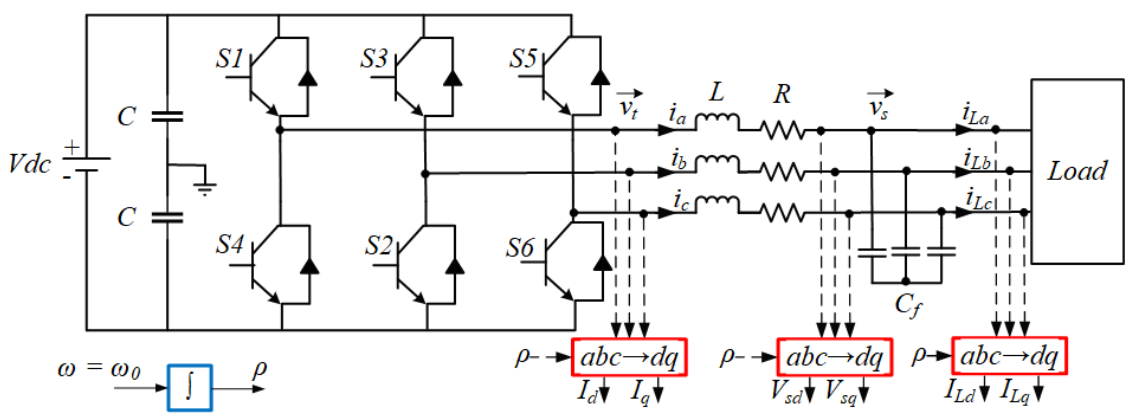

Figure 3.10: Controlled-Frequency VSC System.

3.6.1 Dynamic Model of Load Voltage and Voltage Controller

With reference to Figure 3.10 [84], the load dynamics can be expressed by the following space phasor equation:

$$C_f \frac{d\vec{V_s}}{dt} = \vec{i} - \vec{i_L} \tag{3.34}$$

Similar to the analysis of dynamics in the grid-imposed frequency case, using the dq-transformation $\vec{f} = f_{dq}e^{j\rho}$ and splitting the resultant into real and imaginary parts, it can be obtained:

$$C_f \frac{dV_{sd}}{dt} = C_f(\omega V_{sq}) + i_d - i_{Ld} \tag{3.35}$$

$$C_f \frac{dV_{sq}}{dt} = -C_f(\omega V_{sd}) + i_q - i_{Lq} \tag{3.36}$$

These equations emphasize that V_{sd} and V_{sq} are coupled but can be controlled by i_{dref} and i_{qref}. To decouple the dynamics of the load voltage [84], i_{dref} and i_{qref} can be assumed as:

$$i_{dref} = u_d - C_f(\omega V_{sq}) + i_{Ld} \tag{3.37}$$

$$i_{qref} = u_q + C_f(\omega V_{sd}) + i_{Lq} \tag{3.38}$$

In the Laplace domain, they can be expressed as:

$$I_d(s) = \frac{1}{\tau_i s + 1}(U_d(s) - C_f \pounds(\omega V_{sq}) + I_{Ld}(s)) \tag{3.39}$$

$$I_q(s) = \frac{1}{\tau_i s + 1}(U_q(s) + C_f \pounds(\omega V_{sd}) + I_{Lq}(s)) \tag{3.40}$$

where $\pounds()$ symbolizes the Laplace transform operator.

It is noted that $I_d(s) = \frac{1}{\tau_i s+1} I_{dref}(s)$ and $I_q(s) = \frac{1}{\tau_i s+1} I_{qref}(s)$, τ_i is the time constant due to the d- and q-axis compensator tracking property discussed in the grid-imposed frequency VSC system. Thus, substitute i_d and i_q into Equations 3.35 and 3.36, a set of

equations in the Laplace domain of the load voltage dynamics is:

$$C_f s V_{sd}(s) = \frac{1}{\tau_i s + 1} U_d(s) + [C_f \pounds(\omega V_{sq}) - I_{Ld}(s)](1 - \frac{1}{\tau_i s + 1}) \tag{3.41}$$

$$C_f s V_{sq}(s) = \frac{1}{\tau_i s + 1} U_q(s) - [C_f \pounds(\omega V_{sd}) + I_{Lq}(s)](1 - \frac{1}{\tau_i s + 1}) \tag{3.42}$$

The PI transfer function has a unity DC gain. Hence, $1 - 1/(\tau_i s + 1) = \tau_i s/(\tau_i s + 1)$ has a zero DC gain. If τ_i is small, the subtraction $1 - 1/(\tau_i s + 1)$ becomes minor and can be approximated zero [84]. This approximation simplifies the Laplace Equations 3.41 and 3.42 into:

$$\frac{V_{sd}(s)}{U_d(s)} \approx (\frac{1}{\tau_i s + 1}) \frac{1}{C_f s} \tag{3.43}$$

$$\frac{V_{sq}(s)}{U_q(s)} \approx (\frac{1}{\tau_i s + 1}) \frac{1}{C_f s} \tag{3.44}$$

These linear decoupled equations demonstrate the possibility of controlling V_{sd} and V_{sq} independently by U_d and U_q, respectively. Thus, a general voltage controller model is built and described in Figure 3.11 [84]:

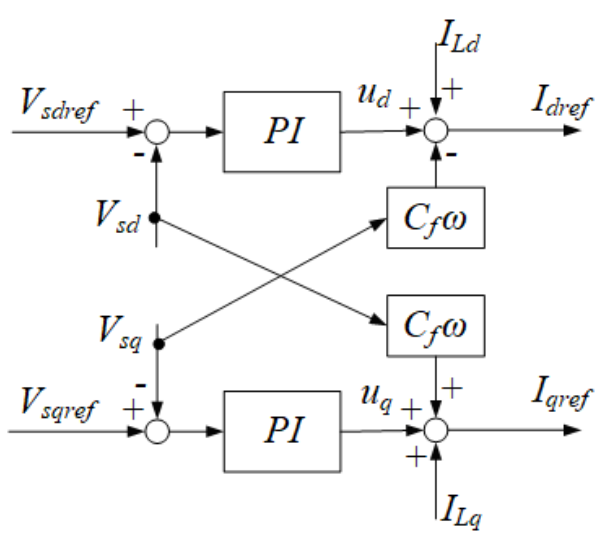

Figure 3.11: Controlled-Frequency Controller Block Diagram.

Figure 3.12 shows an equivalent control loop design comprising a pole at $s = 0$, $s = -1/\tau_i$:

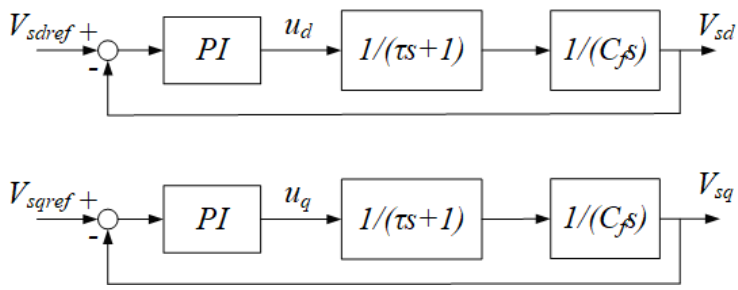

Figure 3.12: Equivalent Controller Block Diagram of Controlled-Frequency VSC System.

The most straightforward compensator to obtain fast regulation and zero steady-state error for this control loop is a PI compensator [84], which is under the formulation of:

$$k(s) = k\frac{s+z}{s} \tag{3.45}$$

The closed-loop transfer function is:

$$T(s) = (\frac{k}{\tau_i C_s})(\frac{1}{s^2})\frac{s+z}{s+\tau_i^{-1}} \tag{3.46}$$

Due to repeated poles at $s = 0$, in frequency response, $\angle l(j\omega) \approx 180^o$. The maximum phase angle δ_m at certain frequency ω_m is described as:

$$\delta_m = sin^{-1}(\frac{1-\tau_i z}{1+\tau_i z}) \tag{3.47}$$

$$\omega_m = \sqrt{z\tau_i^{-1}} \tag{3.48}$$

If the gain crossover frequency ω_c is selected as ω_m, then δ_m is the phase margin. Thus, the compensator proportional gain k must satisfy the condition $|l(j\omega_c)| = |l(j\omega_m)| = 1$. The value of the proportional gain k is:

$$k = C_f\omega_c \tag{3.49}$$

Typically, the phase margin chosen is ranging from 30° to 75°, in which two common options are 45° and 53°. For 45°, we have two repeated poles at $s = -\omega_c$, while for 53°, triple repeated poles are located at $s = -\omega_c$.

From all of the analysis, the controller design diagram for the controlled-frequency VSC system is proposed in Figure 3.13 [84]:

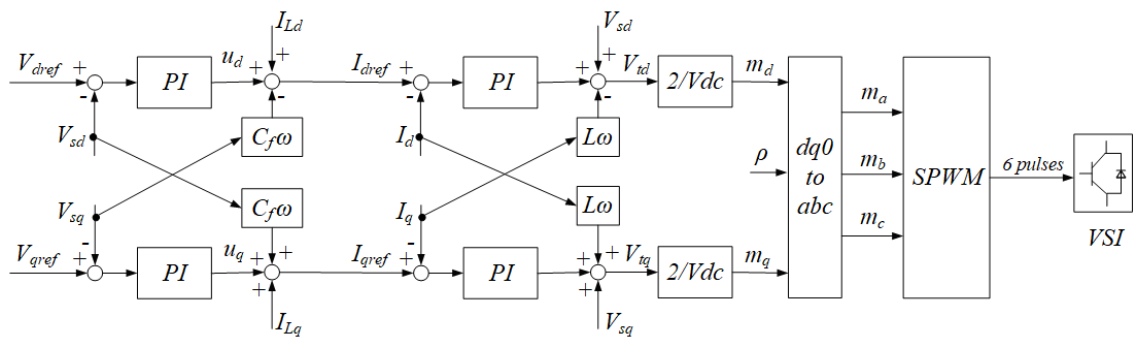

Figure 3.13: Controller Block Diagram of Frequency-Controlled VSC System.

3.7 Virtual Inertia

To mimic the characteristics of a synchronous generator, a control method, inspired by the swing equation, implements the synchronous generator's rotor motion equation. The mechanical component of the synchronous generator is governed by:

$$J\ddot{\theta} = T_m - T_e + D_p\dot{\theta} \tag{3.50}$$

where T_m is the mechanical torque, T_e is the electromagnetic torque, J is the momentum of inertia of all parts when they are rotating with the rotor, D_p is the damping coefficient, θ is the rotor position.

It is known that the acceleration $\ddot{\theta}$ is the derivation of the angular frequency ω, and the instantaneous power of an angularly accelerating body is the torque times the angular velocity, which means $P = T\omega$. Thus, the power-frequency swing equation can be derived as:

$$J\frac{d\omega}{dt} = \frac{P_m - P_e}{\omega_N} + D\Delta\omega \tag{3.51}$$

where P_m is the active input power emulating the mechanical power of a synchronous generator, P_e is active output power simulating the electrical power of a synchronous gen-

erator; ω is the virtual angular frequency, ω_N is the rated angular frequency, which is either 60/50Hz depending on the operating frequency of each specific system, ω_g is the grid/reference angular frequency, $\Delta\omega = \omega_N - \omega_g$. Typically, for a physical synchronous generator, its moment of inertia and the damping coefficient are almost constant values. Nevertheless, due to the control purpose of obtaining an effective dynamic response, moment of inertia and damping factor in virtual inertia emulation can be altered in real-time.

Based on Equation 3.51, a virtual inertia controller diagram can be designed in the Laplace domain and is shown in Figure 3.14:

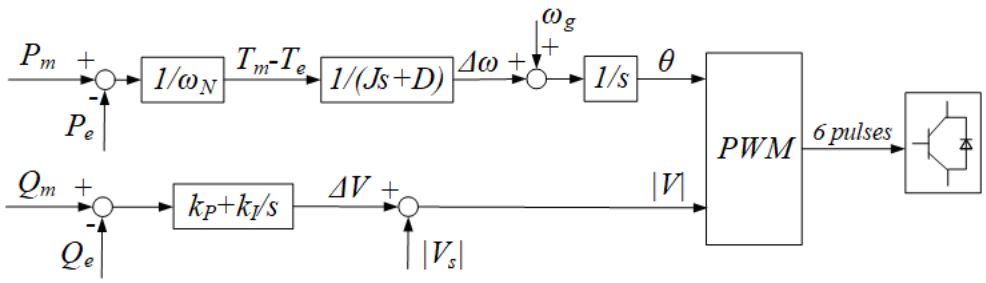

Figure 3.14: Controller Block Diagram of Swing Equation-Based Method in Grid-Connected Mode.

The electrical output active power of VSC, P_e, and the grid angular frequency signals at the PCC are measured and sent to the controller. It takes a setting value of the mechanical power P_m to deduct with the measured signal of the electrical output power P_e and divides this subtraction by the rated angular frequency to generate the difference between the mechanical and electromagnetic torque. The multiplication of $D\Delta\omega$ is added with this torque difference. This multiplication is passed through an integration block with a factor of $1/J$ to find the virtual angular frequency ω. This virtual angular frequency is again passed through an integration block to generate the final output of the controller θ, which is the phase command for the PWM generator. The voltage reference V can be produced by the $Q - V$ droop approach.

In the islanded mode, a simple model of virtual inertia inspired by the momentum of

inertia J and damping factor D in the swing equation can be implemented into the VCO:

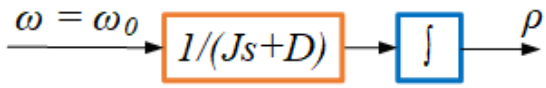

Figure 3.15: Simplified Controller Block Diagram of Swing Equation-Based Method in Islanded Mode.

CHAPTER 4

PERFORMANCE EVALUATION

Chapter 4 presents the simulation results and analysis of virtual inertia implemented in the MATLAB/Simulink environment. The simulation is carried out in the grid-connected and islanded mode. The power and voltage control performances are presented and analyzed. Performances of the systems under fault conditions are also tested.

4.1 SIMULATION OF GRID-CONNECTED INVERTER WITH VIRTUAL INERTIA

For the control and stability analysis of the grid-connected system with virtual inertia implementation inspired by the swing equation, a three-phase inverter system, with a DC voltage source $V_{DC} = 30kV$, a series branch RL with $R = 0.1\Omega$, $L = 5mH$, a switching frequency $f_{sw} = 1620Hz$, is connected to the grid with the operating frequency $f = 60Hz$. The system controller is described in Figure 3.14.

Table 4.1: Simulation Parameters in Grid-Connected Mode

Notation	**Parameter**	**Value**
V_{DC}	DC voltage	$30kV$
R	Connection resistance	0.1Ω
L	Filter inductance	$5mH$
f_{sw}	Switching frequency	$1620Hz$
f	Operating frequency	$60Hz$
J	Moment of inertia	$0.001kgm^2$
D	Damping factor	0.01 $kgms^{-2}$
k_P	Proportional gain	1
k_I	Integral gain	10
V	Phase to phase grid voltage	$13.8kV$

Active and reactive power references are set as $10MW$ and $0var$, respectively. As

shown in Figures 4.1 and 4.2, the controller has been proven to control the active and reactive power injected to the grid successfully.

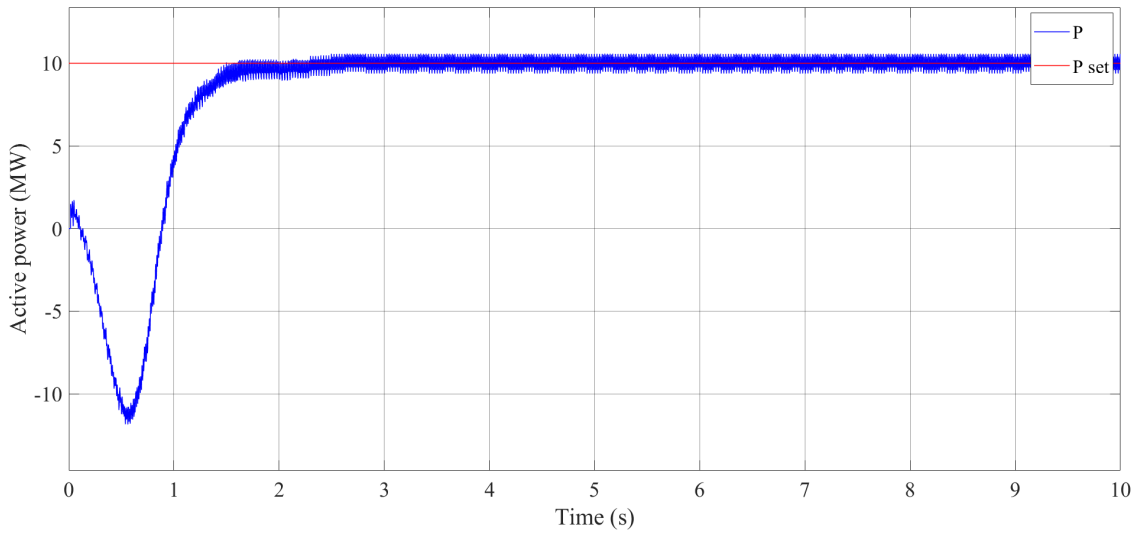

Figure 4.1: Active Power Control in Grid-Connected System.

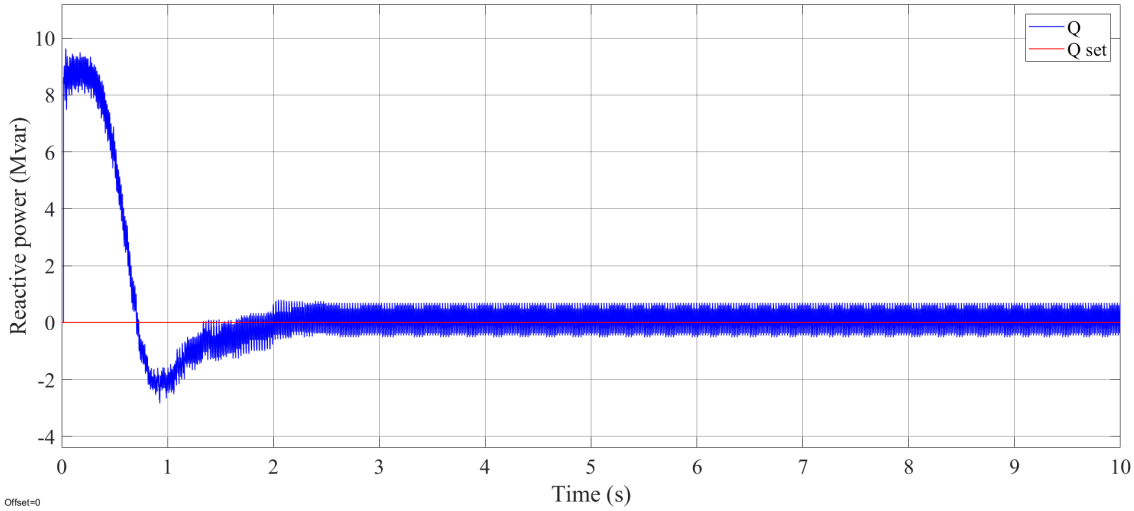

Figure 4.2: Reactive Power Control in Grid-Connected System.

Simulation of the grid-connected system is carried out under different short-circuit fault types for two intervals, half a cycle (1/120s) and six cycles (0.1s). According to the graphs, the system needs approximately 0.02s to recover its performance after a fault removal. Simulation results for half-a-cycle fault duration, starting at 1.2s, are shown below:

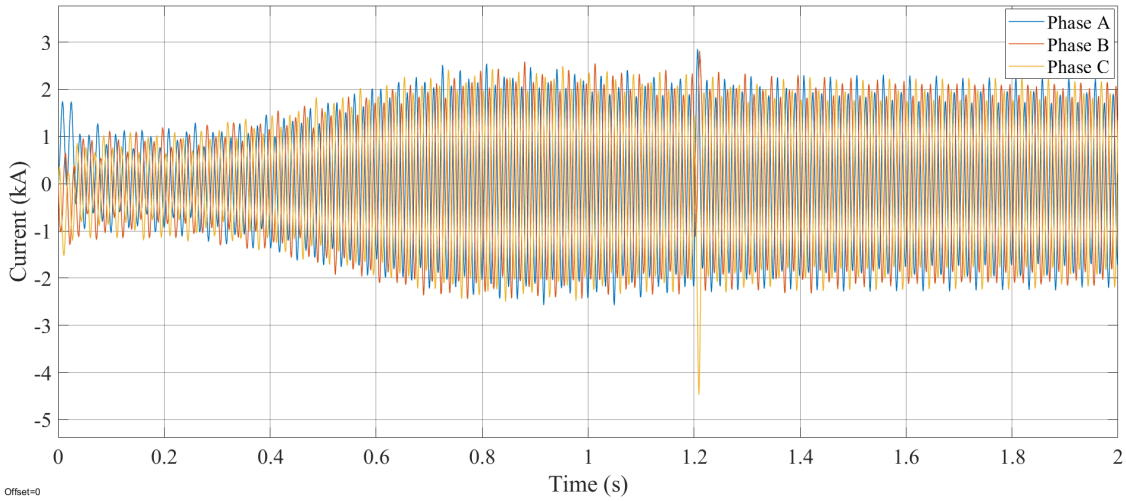

Figure 4.3: Current Generated by Inverter under Line-To-Line-To-Line-To-Ground (LLLG) Half-A-Cycle Fault in Grid-Connected Mode.

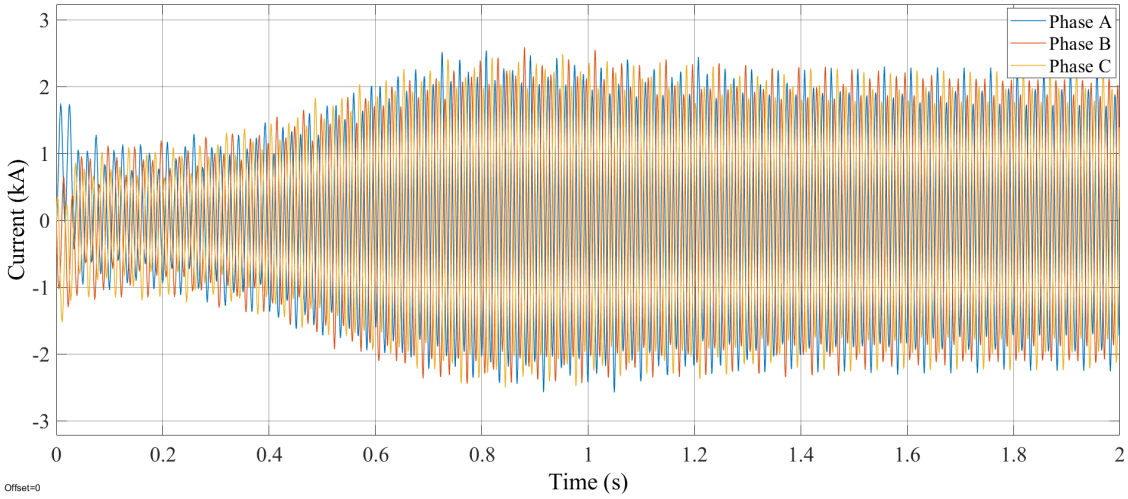

Figure 4.4: Current Generated by Inverter under Line-To-Ground (LG) Half-A-Cycle Fault in Grid-Connected Mode.

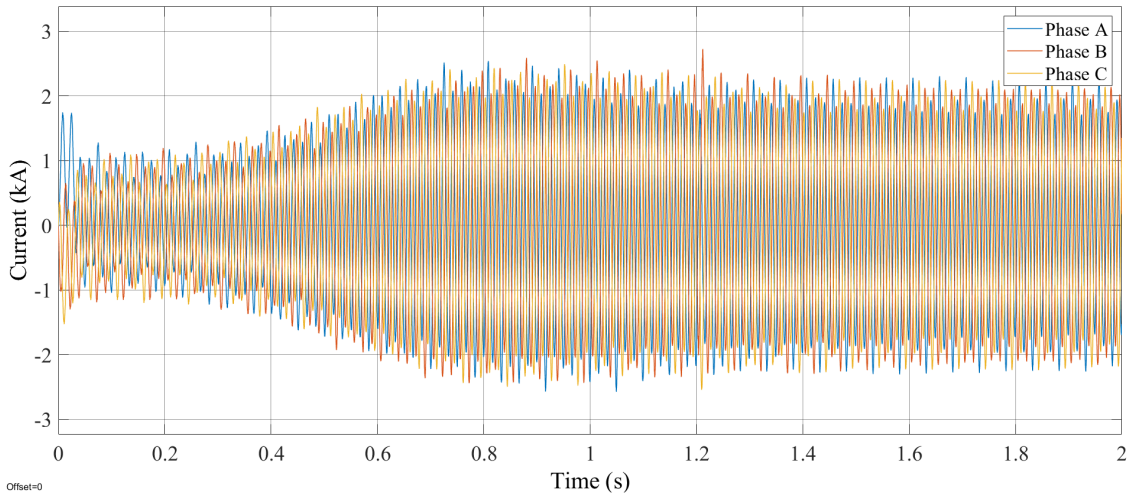

Figure 4.5: Current Generated by Inverter under Double Line-To-Ground (LLG) Half-A-Cycle Fault in Grid-Connected Mode.

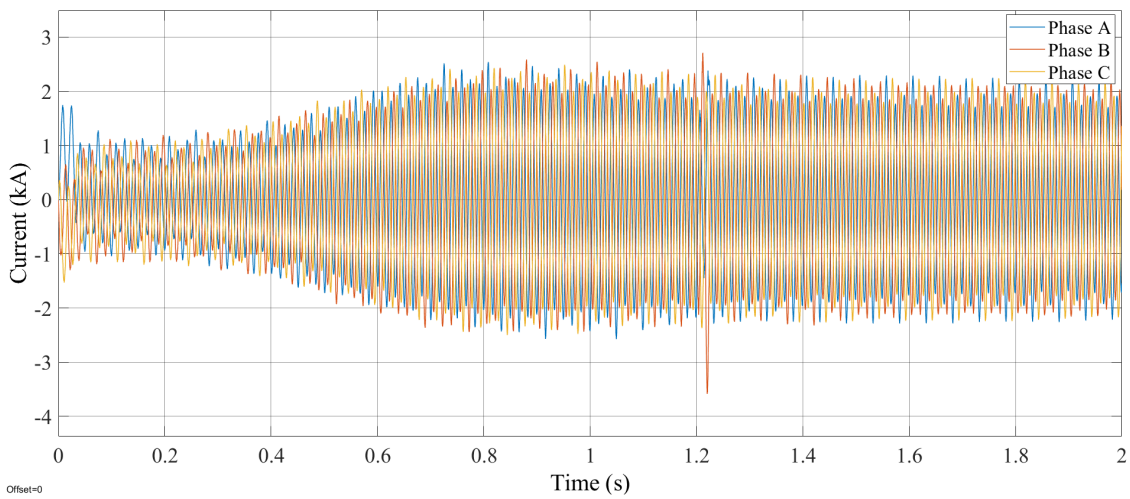

Figure 4.6: Current Generated by Inverter under Line-To-Line (LL) Half-A-Cycle Fault in Grid-Connected Mode.

Next, simulation results for six-cycle fault duration, starting at 1.2s, are shown below:

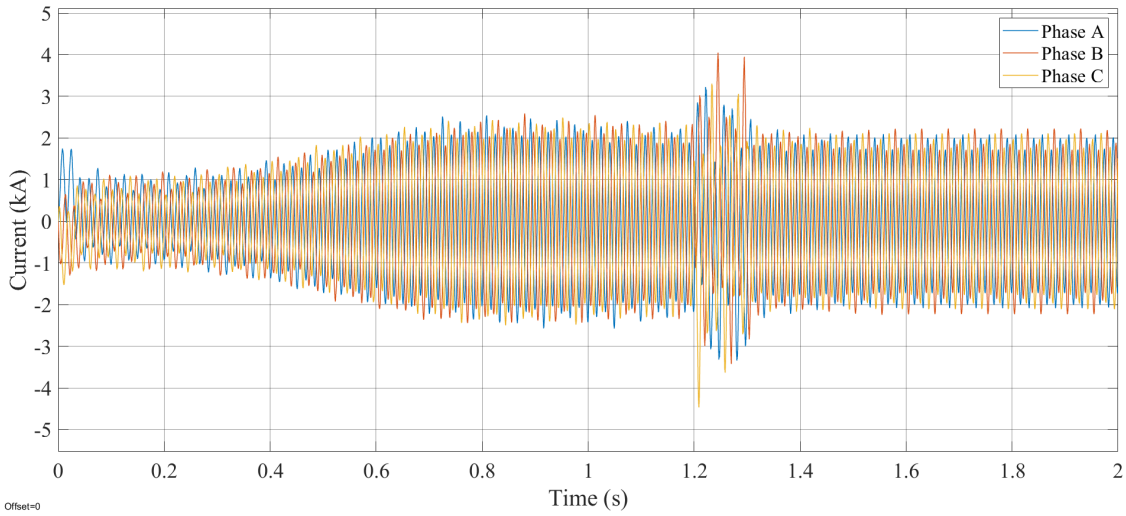

Figure 4.7: Current Generated by Inverter under Line-To-Line-To-Line-To-Ground (LLLG) Six-Cycle Fault in Grid-Connected Mode.

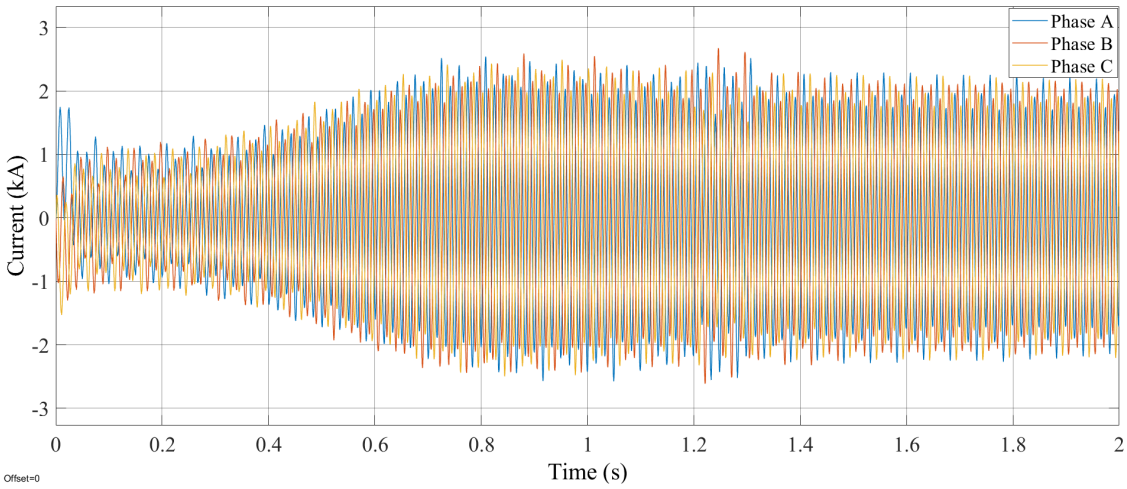

Figure 4.8: Current Generated by Inverter under Line-To-Ground (LG) Six-Cycle Fault in Grid-Connected Mode.

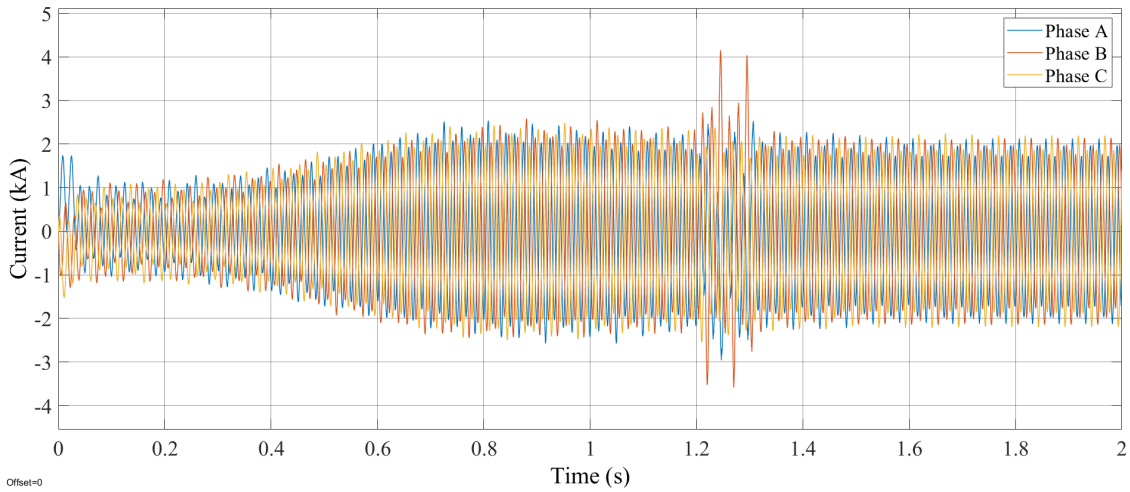

Figure 4.9: Current Generated by Inverter under Line-To-Line-To-Ground (LLG) Six-Cycle Fault in Grid-Connected Mode.

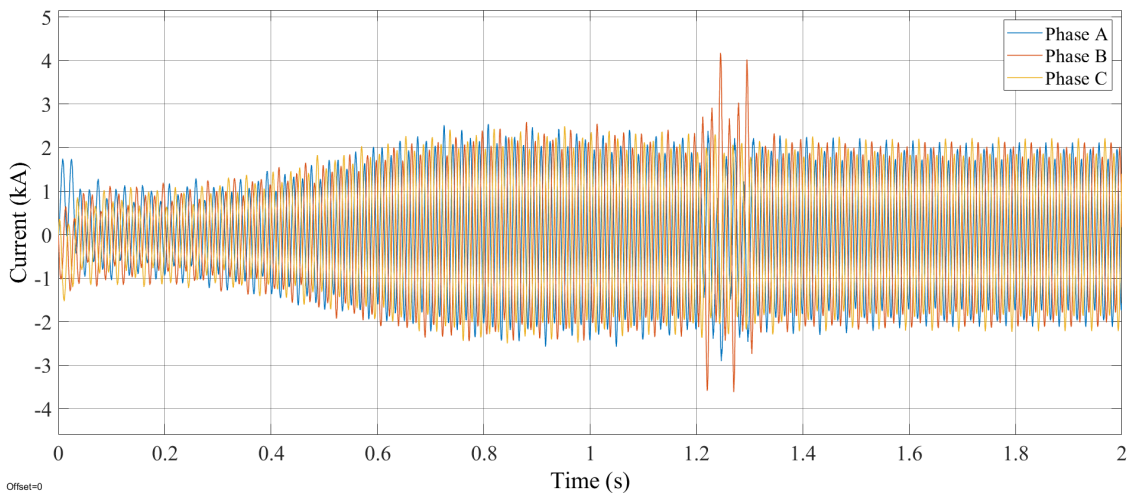

Figure 4.10: Current Generated by Inverter under Line-To-Line (LL) Six-Cycle Fault in Grid-Connected Mode.

4.2 Simulation of Islanded Inverter with Virtual Inertia

For the control and stability analysis of the islanded system with a simplified virtual inertia implementation, a three-phase inverter system, with a DC voltage source $V_{DC} = 800V$, $R = 0.1915\Omega$, $L = 0.0192H$, $f_{sw} = 8100Hz$, is connected to the grid with the operating frequency $f = 60Hz$.

Table 4.2: Simulation Parameters in Islanded Mode

Notation	Parameter	Value
V_{DC}	DC voltage	$800V$
R	Connection resistance	0.1915Ω
L	Filter inductance	$0.0192H$
C_f	Filter capacitance	$9.1848\mu F$
f_{sw}	Switching frequency	$8100Hz$
f	Operating frequency	$60Hz$
J	Moment of inertia	$0.001kgm^2$
D	Damping factor	$1\ kgms^{-2}$
k_{P1}	Proportional gain of inner current control loop	0.9576
k_{I2}	Integral gain of inner current control loop	9.5758
k_{P2}	Proportional gain of voltage outer control loop	0.0308
k_{I2}	Integral gain of voltage outer control loop	3.4587
V	Phase to phase grid voltage	$13.8kV$

The system controller is described and simulated based on Figure 3.13. V_d and V_q references are set as $300V$ and $50V$, respectively. As can be seen from Figures 4.11 and 4.12, the controller has been proven to control the voltage supplied to the load successfully.

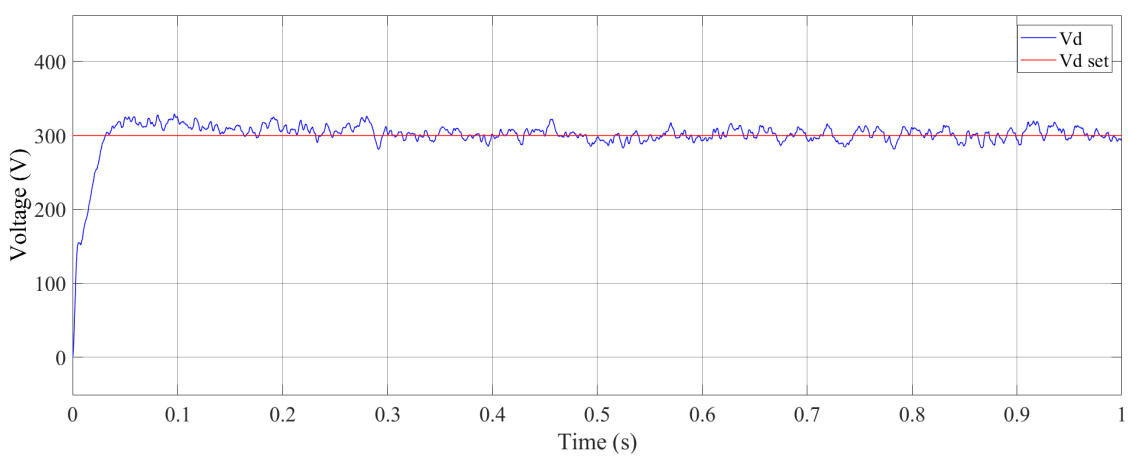

Figure 4.11: V_d Component Control in Islanded System.

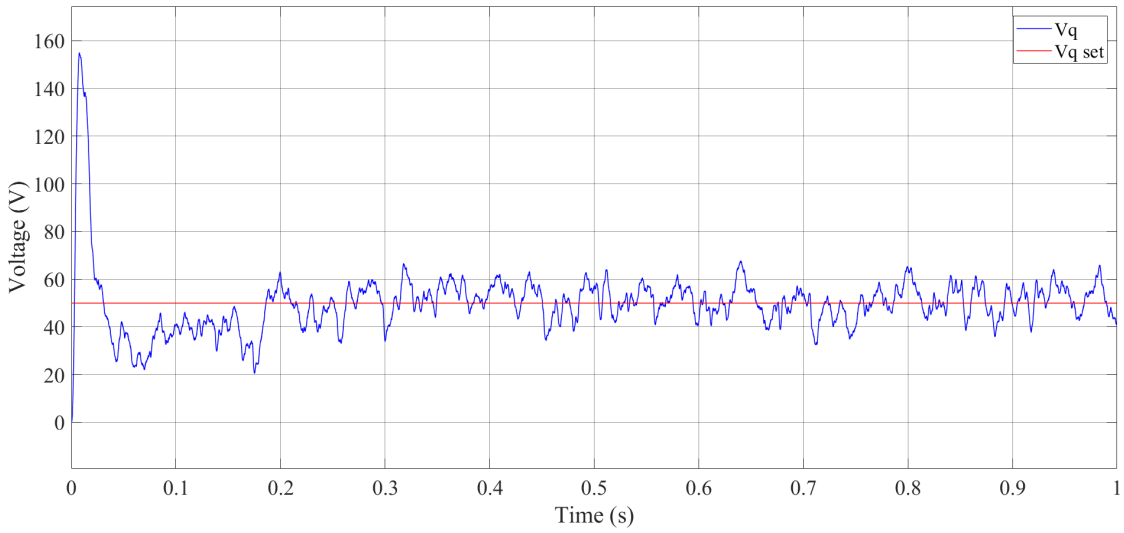

Figure 4.12: V_q Component Control in Islanded System. .

Figure 4.13 illustrates the loop-gain magnitude and phase plots of the load voltage regulator using the compensator in Equation 3.45. Figure 4.13 shows that the phase margin is 53^0 at $\omega_c = 335.182 rad/s$, which is true with respect to the calculation in Equations 3.47 and 3.48.

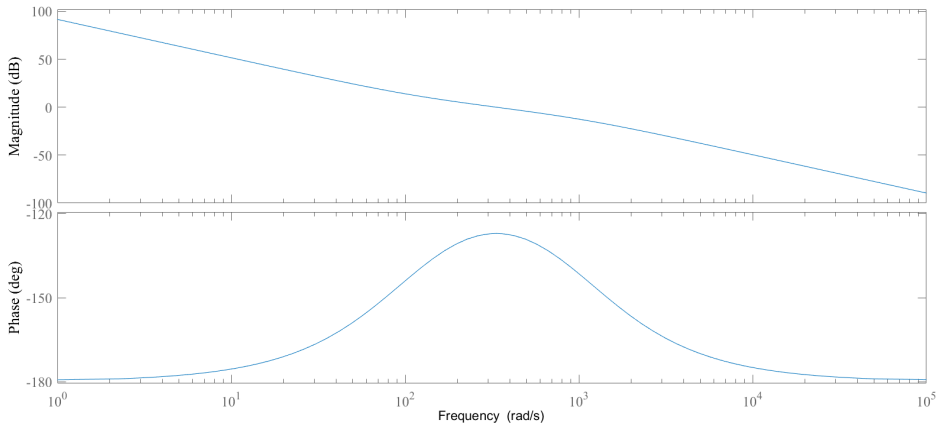

Figure 4.13: Bode Plot of Voltage Control Open-Loop Function.

Simulation of the grid-connected system is carried out under different short-circuit fault types for two intervals, half a cycle (1/120s) and six cycles (0.1s). According to the graphs, the system needs approximately 0.15s to recover its performance after a fault re-

moval. Simulation results for half-a-cycle fault duration, starting at 1.2s, are shown below:

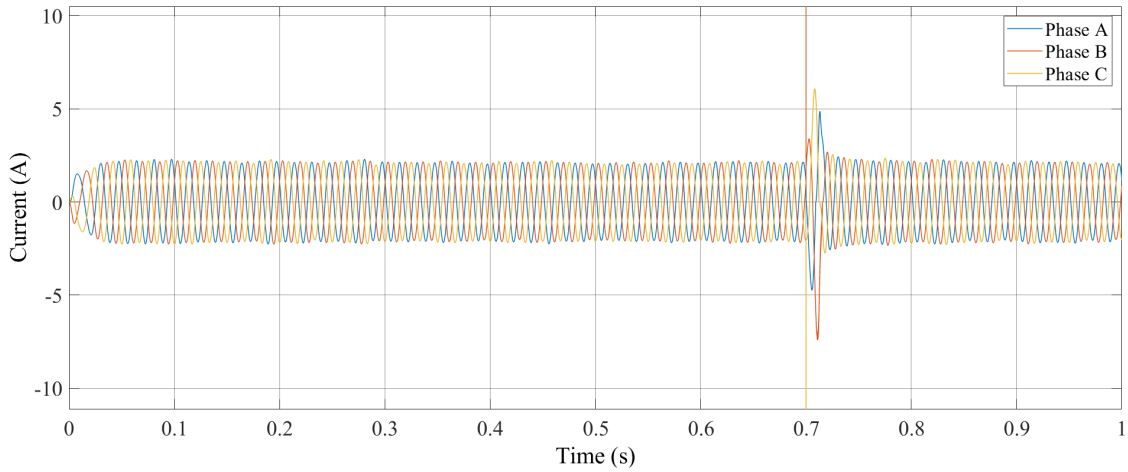

Figure 4.14: Current Generated by Inverter under Line-To-Line-To-Line-To-Ground (LLLG) Half-A-Cycle Fault in Islanded Mode.

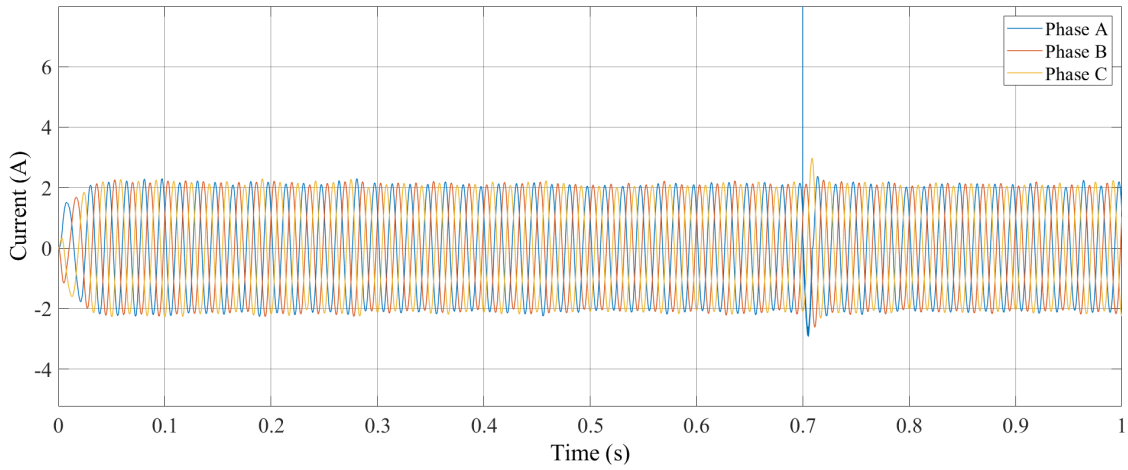

Figure 4.15: Current Generated by Inverter under Line-To-Ground (LG) Half-A-Cycle Fault in Islanded Mode.

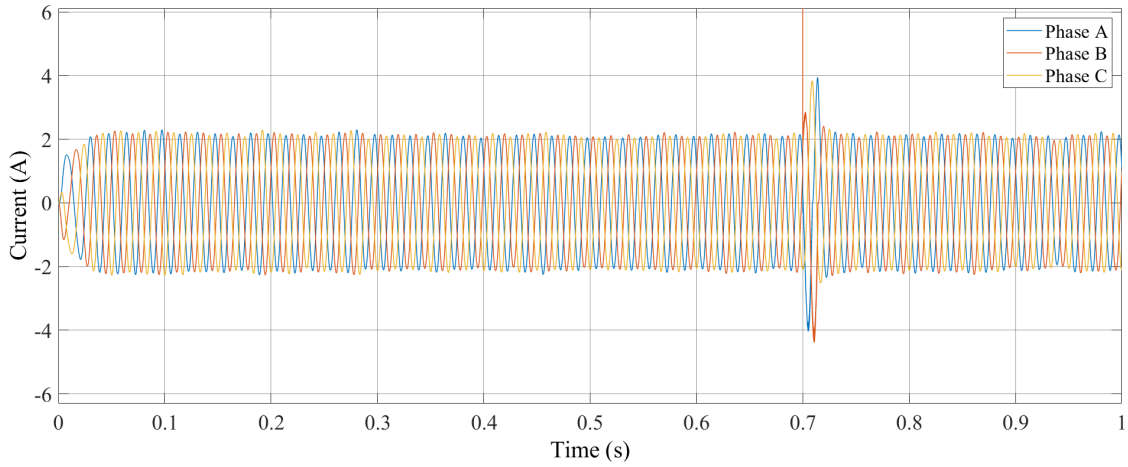

Figure 4.16: Current Generated by Inverter under Double Line-To-Ground (LLG) Half-A-Cycle Fault in Islanded Mode.

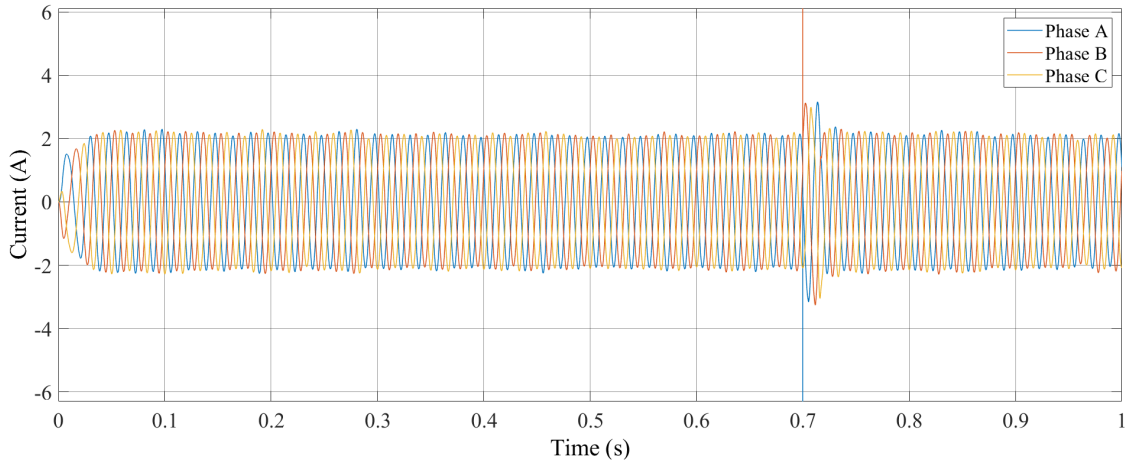

Figure 4.17: Current Generated by Inverter under Line-To-Line (LL) Half-A-Cycle Fault in Islanded Mode.

Next, the simulation results for six-cycle fault duration, starting at 1.2s, are shown below:

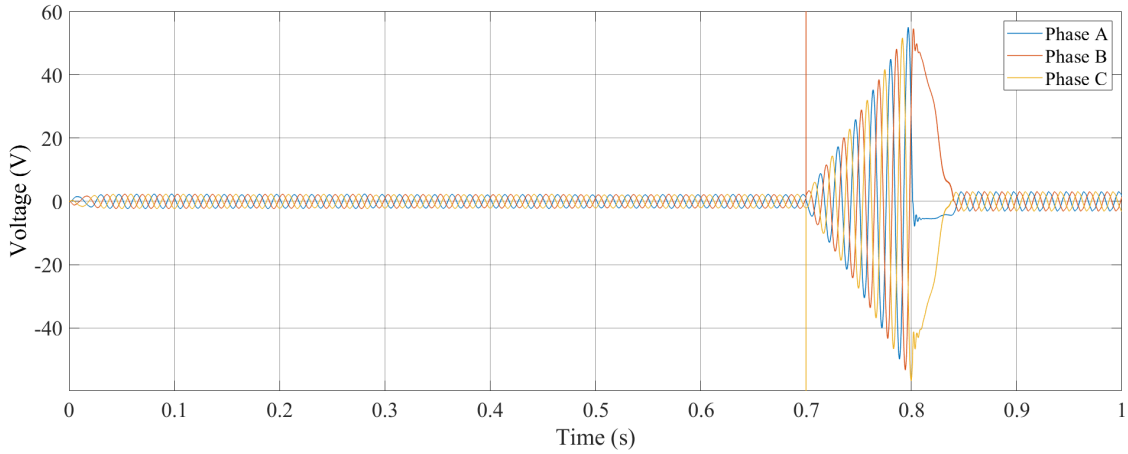

Figure 4.18: Current Generated by Inverter under Line-To-Line-To-Line-To-Ground (LLLG) Six-Cycle Fault in Islanded Mode.

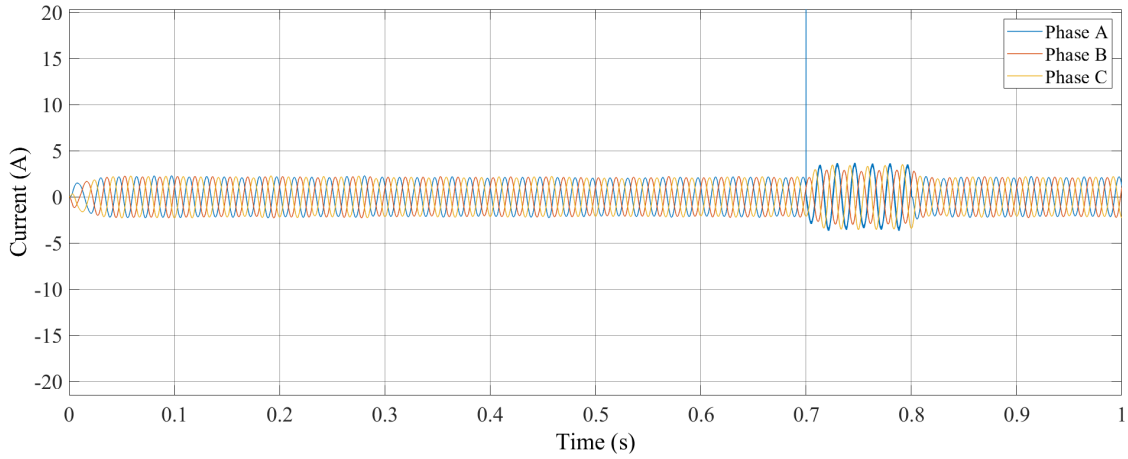

Figure 4.19: Current Generated by Inverter under Line-To-Ground (LG) Six-Cycle Fault in Islanded Mode.

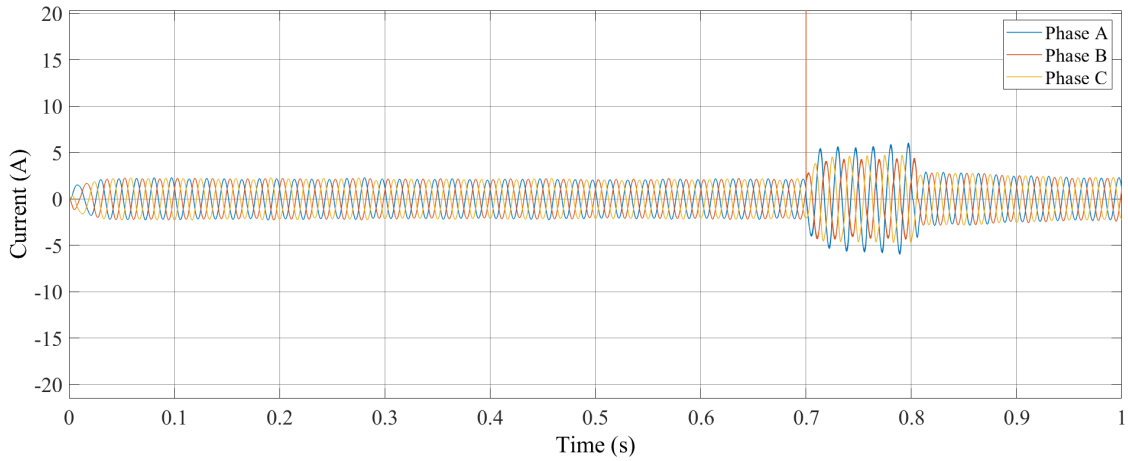

Figure 4.20: Current Generated by Inverter under Double Line-To-Ground (LLG) Six-Cycle Fault in Islanded Mode.

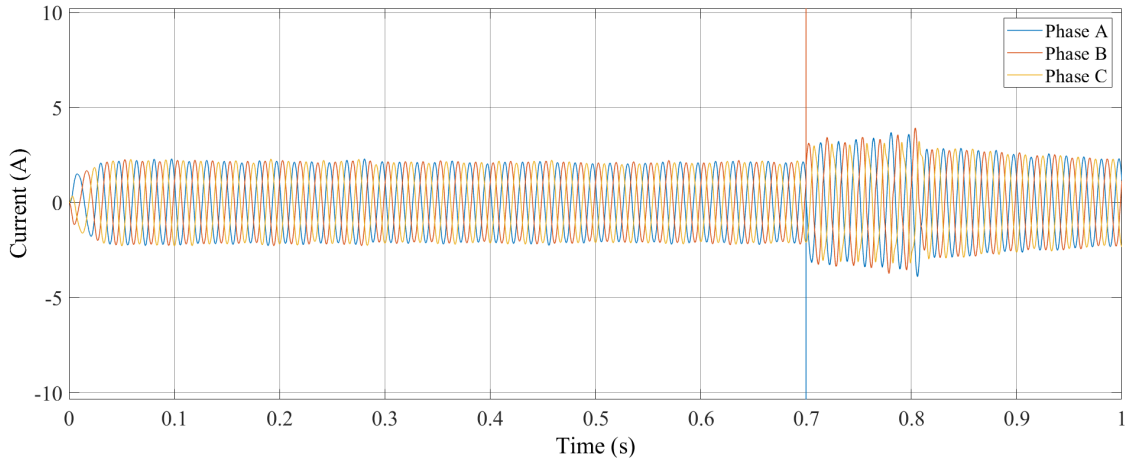

Figure 4.21: Current Generated by Inverter under Line-To-Line (LL) Six-Cycle Fault in Islanded Mode.

CHAPTER 5

CONCLUSIONS AND FUTURE WORKS

In this thesis, a method of creating virtual inertia for an inverter-based system inspired by the swing equation has been proposed. The proposed technique employs the basic swing equation principle to implement the virtual inertia for the grid-connected system. A simplified virtual inertia model for the islanded system is also proposed in addition to the theory of the voltage outer loop and the inner current control loop. The simulation results show that the models have successfully emulated the virtual synchronous machine, with power-sharing capabilities in the grid-connected mode, voltage, and frequency control in the islanded mode. The performances of the systems in two modes of operation reveal the efficiency of the controller.

Future works should include the combination of the current, voltage control loops, and the swing equation in the grid-connected VSC system. Robust control should be investigated as a further implementation of this virtual inertia model, for it to work well under a different set of assumptions.

REFERENCES

[1] A. Qazi, F. Hussain, N. A. Rahim, G. Hardaker, D. Alghazzawi, K. Shaban, and K. Haruna, "Towards sustainable energy: A systematic review of renewable energy sources, technologies, and public opinions," *IEEE Access*, vol. 7, pp. 63 837–63 851, 2019.

[2] A. Aghazadeh, M. Davari, H. Nafisi, and F. Blaabjerg, "Grid integration of a dual two-level voltage-source inverter considering grid impedance and phase-locked loop," *IEEE Journal of Emerging and Selected Topics in Power Electronics*, pp. 1–1, 2019.

[3] I. E. Agency, "Renewables 2019," https://www.iea.org/reports/renewables-2019, 2019.

[4] REN21, "Renewables 2019 global status report," https://www.ren21.net/gsr-2019/, 2019.

[5] M. Davari and Y. A. I. Mohamed, "Variable-structure-based nonlinear control for the master vsc in dc-energy-pool multiterminal grids," *IEEE Transactions on Power Electronics*, vol. 29, no. 11, pp. 6196–6213, 2014.

[6] M. F. M. Arani and E. F. El-Saadany, "Implementing virtual inertia in dfig-based wind power generation," *IEEE Transactions on Power Systems*, vol. 28, no. 2, pp. 1373–1384, May 2013.

[7] J. Fang, H. Li, Y. Tang, and F. Blaabjerg, "Distributed power system virtual inertia implemented by grid-connected power converters," *IEEE Transactions on Power Electronics*, vol. 33, no. 10, pp. 8488–8499, Oct 2018.

[8] B. Kroposki, B. Johnson, Y. Zhang, V. Gevorgian, P. Denholm, B. Hodge, and B. Hannegan, "Achieving a 100% renewable grid: Operating electric power systems with extremely high levels of variable renewable energy," *IEEE Power and Energy Magazine*, vol. 15, no. 2, pp. 61–73, March 2017.

[9] R. Yan, T. Saha, N. Modi, N.-A. Masood, and M. Mosadeghy, "The combined effects of high penetration of wind and pv on power system frequency response," *Applied Energy*, vol. 145, 05 2015.

[10] G. Delille, B. Francois, and G. Malarange, "Dynamic frequency control support by energy storage to reduce the impact of wind and solar generation on isolated power system's inertia," *IEEE Transactions on Sustainable Energy*, vol. 3, no. 4, pp. 931–939, Oct 2012.

[11] F. Blaabjerg, R. Teodorescu, M. Liserre, and A. V. Timbus, "Overview of control and grid synchronization for distributed power generation systems," *IEEE Transactions on Industrial Electronics*, vol. 53, no. 5, pp. 1398–1409, Oct 2006.

[12] U. Tamrakar, D. Shrestha, M. Maharjan, B. Bhattarai, T. Hansen, and R. Tonkoski, "Virtual inertia: Current trends and future directions," *Applied Sciences*, vol. 7, p. 654, 06 2017.

[13] S. D'Arco and J. A. Suul, "Virtual synchronous machines - classification of implementations and analysis of equivalence to droop controllers for microgrids," in *2013 IEEE Grenoble Conference*, June 2013, pp. 1–7.

[14] H. Beck and R. Hesse, "Virtual synchronous machine," in *2007 9th International Conference on Electrical Power Quality and Utilisation*, Oct 2007, pp. 1–6.

[15] Y. Chen, R. Hesse, D. Turschner, and H. Beck, "Investigation of the virtual synchronous machine in the island mode," in *2012 3rd IEEE PES Innovative Smart Grid Technologies Europe (ISGT Europe)*, Oct 2012, pp. 1–6.

[16] Y. Chen, R. Hesse, D. Turschner, and H.-P. Beck, "Dynamic properties of the virtual synchronous machine (visma)," *Renewable Energy and Power Quality Journal*, 05 2011.

[17] H. Bevrani, T. Ise, and Y. Miura, "Virtual synchronous generators: A survey and new perspectives," *International Journal of Electrical Power and Energy Systems*, vol. 54, pp. 244–254, 01 2014.

[18] Y. Hirase, K. Abe, K. Sugimoto, and Y. Shindo, "A grid connected inverter with virtual synchronous generator model of algebraic type," *IEEJ Transactions on Power and Energy*, vol. 132, pp. 371–380, 01 2012.

[19] Q. Zhong and G. Weiss, "Synchronverters: Inverters that mimic synchronous generators," *IEEE Transactions on Industrial Electronics*, vol. 58, no. 4, pp. 1259–1267, April 2011.

[20] Q. Zhong, "Virtual synchronous machines: A unified interface for grid integration," *IEEE Power Electronics Magazine*, vol. 3, no. 4, pp. 18–27, Dec 2016.

[21] Q. Zhong, P. Nguyen, Z. Ma, and W. Sheng, "Self-synchronized synchronverters: Inverters without a dedicated synchronization unit," *IEEE Transactions on Power Electronics*, vol. 29, no. 2, pp. 617–630, Feb 2014.

[22] M. Dewadasa, A. Ghosh, and G. Ledwich, "Dynamic response of distributed generators in a hybrid microgrid," in *2011 IEEE Power and Energy Society General Meeting*, July 2011, pp. 1–8.

[23] C. Zhang, Q. Zhong, J. Meng, X. Chen, Q. Huang, S. Chen, and Z. Lv, "An improved synchronverter model and its dynamic behaviour comparison with synchronous generator," in *2nd IET Renewable Power Generation Conference (RPG 2013)*, 2013, pp. 1–4.

[24] L. Harnefors, M. Bongiorno, and S. Lundberg, "Input-admittance calculation and shaping for controlled voltage-source converters," *IEEE Transactions on Industrial Electronics*, vol. 54, no. 6, pp. 3323–3334, Dec 2007.

[25] D. Jovcic, L. A. Lamont, and L. Xu, "Vsc transmission model for analytical studies," in *2003 IEEE Power Engineering Society General Meeting (IEEE Cat. No.03CH37491)*, vol. 3, July 2003, pp. 1737–1742 Vol. 3.

[26] L. Zhang, L. Harnefors, and H. Nee, "Power-synchronization control of grid-connected voltage-source converters," *IEEE Transactions on Power Systems*, vol. 25, no. 2, pp. 809–820, May 2010.

[27] Y. F. Wang and Y. W. Li, "Grid synchronization pll based on cascaded delayed signal cancellation," *IEEE Transactions on Power Electronics*, vol. 26, no. 7, pp. 1987–1997, July 2011.

[28] K. Lee, J. Lee, D. Shin, D. Yoo, and H. Kim, "A novel grid synchronization pll method based on adaptive low-pass notch filter for grid-connected pcs," *IEEE Transactions on Industrial Electronics*, vol. 61, no. 1, pp. 292–301, Jan 2014.

[29] A. H. Norouzi and A. M. Sharaf, "Two control schemes to enhance the dynamic performance of the statcom and sssc," *IEEE Transactions on Power Delivery*, vol. 20, no. 1, pp. 435–442, Jan 2005.

[30] Z. Ma, Q. Zhong, and J. D. Yan, "Synchronverter-based control strategies for three-phase pwm rectifiers," in *2012 7th IEEE Conference on Industrial Electronics and Applications (ICIEA)*, July 2012, pp. 225–230.

[31] V. Natarajan and G. Weiss, "Almost global asymptotic stability of a constant field current synchronous machine connected to an infinite bus," in *53rd IEEE Conference on Decision and Control*, 2014, pp. 3272–3279.

[32] ——, "Synchronverters with better stability due to virtual inductors, virtual capacitors, and anti-windup," *IEEE Transactions on Industrial Electronics*, vol. 64, no. 7, pp. 5994–6004, 2017.

[33] S. Dong and Y. C. Chen, "Adjusting synchronverter dynamic response speed via damping correction loop," *IEEE Transactions on Energy Conversion*, vol. 32, no. 2, pp. 608–619, 2017.

[34] G. C. Konstantopoulos, Q. . Zhong, B. Ren, and M. Krstic, "Bounded integral control of input-to-state practically stable nonlinear systems to guarantee closed-loop stability," *IEEE Transactions on Automatic Control*, vol. 61, no. 12, pp. 4196–4202, 2016.

[35] Q. Zhong, G. C. Konstantopoulos, B. Ren, and M. Krstic, "Improved synchronverters with bounded frequency and voltage for smart grid integration," *IEEE Transactions on Smart Grid*, vol. 9, no. 2, pp. 786–796, 2018.

[36] G. C. Konstantopoulos, Q. Zhong, B. Ren, and M. Krstic, "Boundedness of synchronverters," in *2015 European Control Conference (ECC)*, 2015, pp. 1050–1055.

[37] K. Sakimoto, Y. Miura, and T. Ise, "Stabilization of a power system with a distributed generator by a virtual synchronous generator function," in *8th International Conference on Power Electronics - ECCE Asia*, May 2011, pp. 1498–1505.

[38] J. Machowski, J. Bialek, and J. Bumby, "Power system dynamics and stability and control," 01 2012.

[39] J. Alipoor, Y. Miura, and T. Ise, "Power system stabilization using virtual synchronous generator with alternating moment of inertia," *IEEE Journal of Emerging and Selected Topics in Power Electronics*, vol. 3, no. 2, pp. 451–458, June 2015.

[40] Jia Liu, Y. Miura, and T. Ise, "Dynamic characteristics and stability comparisons between virtual synchronous generator and droop control in inverter-based distributed

generators," in *2014 International Power Electronics Conference (IPEC-Hiroshima 2014 - ECCE ASIA)*, May 2014, pp. 1536–1543.

[41] K. Sakimoto, Y. Miura, and T. Ise, "Characteristics of parallel operation of inverter type distributed generators operated by a virtual synchronous generator," *IEEJ Transactions on Power and Energy*, vol. 133, pp. 186–194, 01 2013.

[42] S. Silwal, S. Taghizadeh, M. Karimi-Ghartemani, M. J. Hossain, and M. Davari, "An enhanced control system for single-phase inverters interfaced with weak and distorted grids," *IEEE Transactions on Power Electronics*, vol. 34, no. 12, pp. 12 538–12 551, 2019.

[43] M. Davari and Y. A. I. Mohamed, "Robust dc-link voltage control of a full-scale pmsg wind turbine for effective integration in dc grids," *IEEE Transactions on Power Electronics*, vol. 32, no. 5, pp. 4021–4035, 2017.

[44] P. Rodriguez, I. Candela, and A. Luna, "Control of pv generation systems using the synchronous power controller," in *2013 IEEE Energy Conversion Congress and Exposition*, Sep. 2013, pp. 993–998.

[45] P. Rodriguez, I. Candela, C. Citro, J. Rocabert, and A. Luna, "Control of grid-connected power converters based on a virtual admittance control loop," in *2013 15th European Conference on Power Electronics and Applications (EPE)*, Sep. 2013, pp. 1–10.

[46] W. Zhang, A. M. Cantarellas, J. Rocabert, A. Luna, and P. Rodriguez, "Synchronous power controller with flexible droop characteristics for renewable power generation systems," *IEEE Transactions on Sustainable Energy*, vol. 7, no. 4, pp. 1572–1582, Oct 2016.

[47] W. Zhang, D. Remon, A. Mir, A. Luna, J. Rocabert, I. Candela, and P. Rodriguez, "Comparison of different power loop controllers for synchronous power controlled grid-interactive converters," in *2015 IEEE Energy Conversion Congress and Exposition (ECCE)*, Sep. 2015, pp. 3780–3787.

[48] J. Liu, Y. Miura, H. Bevrani, and T. Ise, "Enhanced virtual synchronous generator control for parallel inverters in microgrids," *IEEE Transactions on Smart Grid*, vol. 8, no. 5, pp. 2268–2277, 2017.

[49] C. A. C. Coello, G. B. Lamont, and D. A. V. Veldhuizen, *Evolutionary Algorithms for*

Solving Multi-Objective Problems (Genetic and Evolutionary Computation). Berlin, Heidelberg: Springer-Verlag, 2006.

[50] J. Alipoor, Y. Miura, and T. Ise, "Stability assessment and optimization methods for microgrid with multiple vsg units," *IEEE Transactions on Smart Grid*, vol. 9, no. 2, pp. 1462–1471, 2018.

[51] M. Torres and L. A. C. Lopes, "Virtual synchronous generator control in autonomous wind-diesel power systems," in *2009 IEEE Electrical Power Energy Conference (EPEC)*, Oct 2009, pp. 1–6.

[52] T. V. Van, K. Visscher, J. Diaz, V. Karapanos, A. Woyte, M. Albu, J. Bozelie, T. Loix, and D. Federenciuc, "Virtual synchronous generator: An element of future grids," in *2010 IEEE PES Innovative Smart Grid Technologies Conference Europe (ISGT Europe)*, Oct 2010, pp. 1–7.

[53] M. P. N. van Wesenbeeck, S. W. H. de Haan, P. Varela, and K. Visscher, "Grid tied converter with virtual kinetic storage," in *2009 IEEE Bucharest PowerTech*, June 2009, pp. 1–7.

[54] M. Torres and L. Lopes, "Virtual synchronous generator: A control strategy to improve dynamic frequency control in autonomous power systems," *Energy and Power Engineering*, vol. 05, pp. 32–38, 01 2013.

[55] U. Tamrakar, R. Tonkoski, Zhen Ni, T. M. Hansen, and I. Tamrakar, "Current control techniques for applications in virtual synchronous machines," in *2016 IEEE 6th International Conference on Power Systems (ICPS)*, March 2016, pp. 1–6.

[56] V. Karapanos, S. de Haan, and K. Zwetsloot, "Real time simulation of a power system with vsg hardware in the loop," in *IECON 2011 - 37th Annual Conference of the IEEE Industrial Electronics Society*, Nov 2011, pp. 3748–3754.

[57] J. Morren, J. Pierik, and S. Haan, "Inertial response of variable speed wind turbines," *Electric Power Systems Research*, vol. 76, pp. 980–987, 07 2006.

[58] B. Wen, D. Boroyevich, R. Burgos, P. Mattavelli, and Z. Shen, "Small-signal stability analysis of three-phase ac systems in the presence of constant power loads based on measured d-q frame impedances," *IEEE Transactions on Power Electronics*, vol. 30, no. 10, pp. 5952–5963, Oct 2015.

[59] M. Ashabani, F. D. Freijedo, S. Golestan, and J. M. Guerrero, "Inducverters: Pll-less converters with auto-synchronization and emulated inertia capability," *IEEE Transactions on Smart Grid*, vol. 7, no. 3, pp. 1660–1674, May 2016.

[60] T. Midtsund, J. A. Suul, and T. Undeland, "Evaluation of current controller performance and stability for voltage-source converters connected to a weak grid," in *The 2nd International Symposium on Power Electronics for Distributed Generation Systems*, June 2010, pp. 382–388.

[61] W. Guo, F. Liu, J. Si, and S. Mei, "Incorporating approximate dynamic programming-based parameter tuning into pd-type virtual inertia control of dfigs," in *The 2013 International Joint Conference on Neural Networks (IJCNN)*, 2013, pp. 1–8.

[62] M. A. Torres L., L. A. C. Lopes, L. A. MorÃ¡n T., and J. R. Espinoza C., "Self-tuning virtual synchronous machine: A control strategy for energy storage systems to support dynamic frequency control," *IEEE Transactions on Energy Conversion*, vol. 29, no. 4, pp. 833–840, 2014.

[63] D. Shrestha, U. Tamrakar, N. Malla, Zhen Ni, and R. Tonkoski, "Reduction of energy consumption of virtual synchronous machine using supplementary adaptive dynamic programming," in *2016 IEEE International Conference on Electro Information Technology (EIT)*, 2016, pp. 0690–0694.

[64] F. Katiraei and M. R. Iravani, "Power management strategies for a microgrid with multiple distributed generation units," *IEEE Transactions on Power Systems*, vol. 21, no. 4, pp. 1821–1831, Nov 2006.

[65] U. Borup, F. Blaabjerg, and P. N. Enjeti, "Sharing of nonlinear load in parallel-connected three-phase converters," *IEEE Transactions on Industry Applications*, vol. 37, no. 6, pp. 1817–1823, Nov 2001.

[66] M. C. Chandrokar, D. M. Divan, and B. Banerjee, "Control of distributed ups systems," in *Proceedings of 1994 Power Electronics Specialist Conference - PESC'94*, vol. 1, June 1994, pp. 197–204 vol.1.

[67] C. Li, R. Burgos, I. Cvetkovic, D. Boroyevich, L. Mili, and P. Rodriguez, "Analysis and design of virtual synchronous machine based statcom controller," in *2014 IEEE 15th Workshop on Control and Modeling for Power Electronics (COMPEL)*, 2014, pp. 1–6.

[68] S. D'Arco and J. A. Suul, "Equivalence of virtual synchronous machines and frequency-droops for converter-based microgrids," *IEEE Transactions on Smart Grid*, vol. 5, no. 1, pp. 394–395, Jan 2014.

[69] J. M. Guerrero, L. Hang, and J. Uceda, "Control of distributed uninterruptible power supply systems," *IEEE Transactions on Industrial Electronics*, vol. 55, no. 8, pp. 2845–2859, 2008.

[70] Y. A. I. Mohamed and E. F. El-Saadany, "Adaptive decentralized droop controller to preserve power sharing stability of paralleled inverters in distributed generation microgrids," *IEEE Transactions on Power Electronics*, vol. 23, no. 6, pp. 2806–2816, 2008.

[71] J. M. Guerrero, J. C. Vasquez, J. Matas, M. Castilla, and L. Garcia de Vicuna, "Control strategy for flexible microgrid based on parallel line-interactive ups systems," *IEEE Transactions on Industrial Electronics*, vol. 56, no. 3, pp. 726–736, 2009.

[72] M. Davari and Y. A. I. Mohamed, "Robust droop and dc-bus voltage control for effective stabilization and power sharing in vsc multiterminal dc grids," *IEEE Transactions on Power Electronics*, vol. 33, no. 5, pp. 4373–4395, 2018.

[73] J. M. Guerrero, Luis Garcia de Vicuna, J. Matas, M. Castilla, and J. Miret, "Output impedance design of parallel-connected ups inverters with wireless load-sharing control," *IEEE Transactions on Industrial Electronics*, vol. 52, no. 4, pp. 1126–1135, 2005.

[74] J. Kim, J. M. Guerrero, P. Rodriguez, R. Teodorescu, and K. Nam, "Mode adaptive droop control with virtual output impedances for an inverter-based flexible ac microgrid," *IEEE Transactions on Power Electronics*, vol. 26, no. 3, pp. 689–701, 2011.

[75] J. Liu, Y. Miura, and T. Ise, "Comparison of dynamic characteristics between virtual synchronous generator and droop control in inverter-based distributed generators," *IEEE Transactions on Power Electronics*, vol. 31, pp. 3600–3611, 05 2016.

[76] B. B. Johnson, S. V. Dhople, A. O. Hamadeh, and P. T. Krein, "Synchronization of parallel single-phase inverters with virtual oscillator control," *IEEE Transactions on Power Electronics*, vol. 29, no. 11, pp. 6124–6138, Nov 2014.

[77] B. B. Johnson, S. V. Dhople, J. L. Cale, A. O. Hamadeh, and P. T. Krein, "Oscillator-based inverter control for islanded three-phase microgrids," *IEEE Journal of Photovoltaics*, vol. 4, no. 1, pp. 387–395, Jan 2014.

[78] B. B. Johnson, S. V. Dhople, A. O. Hamadeh, and P. T. Krein, "Synchronization of nonlinear oscillators in an lti electrical power network," *IEEE Transactions on Circuits and Systems I: Regular Papers*, vol. 61, no. 3, pp. 834–844, 2014.

[79] D. Chen, Y. Xu, and A. Q. Huang, "Integration of dc microgrids as virtual synchronous machines into the ac grid," *IEEE Transactions on Industrial Electronics*, vol. 64, no. 9, pp. 7455–7466, 2017.

[80] S. R. Awasthi, S. Chalise, and R. Tonkoski, "Operation of datacenter as virtual power plant," in *2015 IEEE Energy Conversion Congress and Exposition (ECCE)*, 2015, pp. 3422–3429.

[81] L. Bajracharyay, S. Awasthi, S. Chalise, T. M. Hansen, and R. Tonkoski, "Economic analysis of a data center virtual power plant participating in demand response," in *2016 IEEE Power and Energy Society General Meeting (PESGM)*, 2016, pp. 1–5.

[82] S. D'Arco, J. Suul, and O. Fosso, "Small-signal modeling and parametric sensitivity of a virtual synchronous machine in islanded operation," *International Journal of Electrical Power & Energy Systems*, vol. 58, 2015.

[83] F. Teng and G. Strbac, "Evaluation of synthetic inertia provision from wind plants," in *2015 IEEE Power Energy Society General Meeting*, 2015, pp. 1–5.

[84] A. Yazdani and R. Iravani, "Voltage-sourced converters in power systems." John Wiley & Sons and IEEE, 2010.

[85] A. Singhal, C. Madhu, and V. Kumar, "Designs of all digital phase locked loop," in *2014 Recent Advances in Engineering and Computational Sciences (RAECS)*, 2014, pp. 1–5.